The Dynamic Role of Gold d-Orbitals During CO Oxidation Under Aerobic Conditions

Alessandro Longo, Francesco Giannici, Maria Casaletto, Mauro Rovezzi, Christoph Sahle, Pieter Glatzel, Yves Joly, Antonino Martorana

The Dynamic Role of Gold d-Orbitals During CO Oxidation Under Aerobic Conditions

Alessandro Longo[1,2*], Francesco Giannici[3], Maria Pia Casaletto[2*], Mauro Rovezzi[1,4], Christoph J. Sahle[1], Pieter Glatzel[1], Yves Joly[5], Antonino Martorana[3].

[1] ESRF - The European Synchrotron, CS 40220, 38043 Grenoble Cedex 9, (France).
[2] Istituto per lo Studio dei Materiali Nanostrutturati, Consiglio Nazionale delle Ricerche, Via Ugo La Malfa 153, 90146 Palermo, (Italy).
[3] Dipartimento di Fisica e Chimica, Università di Palermo, Viale delle Scienze, I - 90128 Palermo, (Italy).
[4] Universitè Grenoble Alpes, CNRS, IRD, Irstea, Météo France, OSUG, FAME, 71 Avenue des Martyrs, CS 40220, 38043, Grenoble (France).
[5] Universitè Grenoble Alpes Inst NEEL, 38042 Grenoble (France) and CNRS, Inst NEEL, 38042 Grenoble (France).

Abstract

High Energy Resolution Fluorescence Detection X-ray Absorption Spectroscopy (HERFD-XANES) at the Au L3 edge was used to study gold catalysts supported on ceria in order to unravel the role of gold 5d orbital modifications during the activation of molecular oxygen. The variations in the HERFD-XANES resonance peak, which are directly correlated with d-band occupancy, were monitored *in situ* during the redox process of the CO oxidation at room temperature both in aerobic and anaerobic conditions.

Interestingly, upon the oxidation treatment and also during the aerobic CO oxidation treatment, the gold *d* band fluctuate around an average value proving that the gold clusters are partially charged. A dynamism of the gold electronic configuration was evidenced by a temporary variation of gold d-

orbitals population during the oxidation reaction.

The interpretation of X-ray spectroscopy data is supported by *ab initio* simulations performed using the FDMNES code.

Keywords: In situ, HERFD, XANES, d-bands, CO oxidation, Au/CeO_2.

Corresponding Authors

* *Alessandro Longo, alessandro.longo@esrf.fr*

* *Maria Pia Casaletto, mariapia.casaletto@cnr.it*

Introduction

CO oxidation on supported gold nanocatalysts has been an emblematic and pivotal problem in catalysis in the last three decades [1-16] and recent literature confirms that it still remains an intriguing subject [12-16]. The presumably simple reaction is challenging to understand because many factors, as the size of the gold particles, the valence state of gold, and gold-support interaction, importantly affect the catalysts activity. All these factors occur together, and disentangling their effects is quite complicate [7, 8, 10, 11]. This issue stimulated a long-standing scientific debate on the nature of the gold active site, resulting in a virtuous synergy between theoretical and experimental works [13,17,18,19]. However, model catalyst systems with controlled gold oxidation states are difficult to obtain, and the description of the real active site for the CO oxidation is still a compelling subject, calling for a direct experimental study of the reaction mechanism under working conditions.

The details in the occupancy of the *d*-band of the supported metal catalyst are pivotal for interpreting and understanding the origin of the catalytic activity [19-22]. The gold catalyzed CO oxidation reaction is usually explained within to the so-called *d*-band model, in which substrate-adsorbate bonds are formed. In this scheme, the position of the *d*-band center plays a fundamental role in the formation and strength of the new bonds. In particular, a *d*-band closer to the Fermi level will give rise a stronger interaction. The center of the *d*-band of bulk gold is situated far below of the Fermi level [19]. However, as soon as the size of gold particles is downsized in the nanometric range (below 5 nm), a significant modification of the electronic structure occurs. In fact, the gold *d*-band center shifts towards energies closer to the Fermi level.

This affects the formed antibonding orbital originated by the interaction of the adsorbed molecule with the metal, whose energy will be finally shifted above the Fermi energy level. Thus, the *d*-band center of gold reduces its

occupancy resulting less filled [19, 22]. In addition to the *d*-band shifts, the very high dispersion of nanosized gold clusters lowers the number of hybridized valence states: this in turn makes the *d*-band states distribution sharper and more defined [13, 19, 23].

In any case, the gold cluster dimension is not the only contributing aspect that has to be considered. The support oxide also directly influences the electronic structure of the supported gold clusters by different mechanisms, e.g. strain-induction and charge transfer [15]. In this respect, a key structural argument used to explain the high activity of metal oxide supported gold clusters relies on the idea of peripheral sites which are formed at the interface between the gold nanoparticle and the oxide [11,15]. These peripheral atoms are supposed to show high activity towards adsorption, due to the higher coordinative unsaturation in comparison with the bulk ones, and to be the preferred sites where the reaction takes place. However, the evidences on gold-catalyzed CO oxidation are still not fully conclusive, and at times even contradictory.

For instance, it was reported that gold octamers clusters (Au8) bound to oxygen-vacancy F-center defects on Mg(001) are the smallest metal gold nanoparticles capable of catalyzing the low-temperature oxidation of CO to CO_2. On the contrary, metal clusters supported on defect-free surfaces are chemically inert. The charging of the deposited clusters plays a key role in promoting their chemical activity [18]. Guo et al. showed that the metallic gold component in clusters are much more important as active sites than Au^+ species for the CO oxidation [14, 16]. Moreover, against the general belief that the active sites are immobile, it was shown that Au clusters are quite flexible during the operating conditions. While large Au nanoparticles effectively remain statically rigid, very small Au clusters lose their internal structures and become almost disordered, inducing considerable sizable rearrangements and resulting in the formation of cyclically "uncoordinated"

atoms on the surface [18]. On the other side, other authors claimed that the single gold atoms dispersed in a reducible defective support are the real active species [24, 25]. Irrespective of all the possible structural scenarios, which are not able to fully explain the electronic modification occurring in the metal particles, it is commonly accepted that the charge transfer, originating from metal-support interaction, produces a local variation in the electronic structure of the gold clusters. Such a modification is mostly located around the cluster itself, or at detached atom sites, and depends strongly on catalyst pre-treatments that may influence the electronic state of gold species ($Au^{\delta+}$, Au^{0}, $Au^{\delta-}$) [26]. The change in metal electronic state allows the π* antibonding orbital of oxygen to interact with the metal *d*-band. As soon as the antibonding orbital occupancy rises, the O=O bond is weakened and elongated, and therefore activated to react with CO [11, 20, 22, 27]. Interestingly, the mechanism by which molecular oxygen is activated on gold particles indicates the transient formation of gold-oxygen complexes [16, 20, 28].

Notably, the activation is detected as an increase of the Au L_3 XANES resonance peak, which indicates the corresponding gold *d*-band occupancy. Nevertheless, important questions concerning the reversibility of the gold-oxygen complex formation, its evolution, and the possible restoration of metal-support interaction during the oxidation process still remain unsolved.

In recent literature, conventional X-ray absorption spectroscopies, which are able to solve the gold local environment in different chemical conditions, are still the main characterization techniques [16, 20-22, 26-29]. The XAFS signal, as it happens for bulk analytical techniques, arises from the combination of all gold atoms. Unfortunately, due to the low resolution achievable in a conventional XAFS experiment, the variations in the *d*-band occupancy (i.e. the XANES region) are hard to be highlighted and interpreted [26, 29]. The high-energy-resolution fluorescence detection (HERFD)

technique can be used to overcome limitations of conventional XAFS techniques, acquiring the intensity of a single fluorescence line corresponding to a specific excited state decay, with the big advantage to have a narrow energy resolution. *In situ* application of HERFD XAFS to several catalytic systems has recently given fundamental insights in structure-properties relationships [30, 31].

In this work, we prepared gold catalysts supported on ceria through the deposition/precipitation method and performed *in situ* HERFD-XANES during the CO oxidation reaction both in anaerobic and aerobic conditions. Ex-situ XRD and XPS characterization provided information on the geometrical structure and surface chemical composition of the catalysts. The variations in the HERFD-XANES showed a clear fluctuating behavior during the oxygen treatments that can be correlated to the corresponding variation in the population of gold *d*-orbitals during the oxidation reaction. Moreover, in aerobic conditions, the *d*-band fluctuates around an intermediate partially empty state which corroborates the dynamic role of the gold clusters during the catalysis.

Modeling of the Au L_3 edge features was performed by ab initio simulations using the Finite Difference Method Near Edge Structure (FDMNES) code [32].

Experimental Section

Catalyst Preparation

Au/CeO_2 powders, with an Au loading of 1.0 and 3.0 % w/w (determined by ICP-AES), were prepared by homogeneous deposition/precipitation method. The urea was used as precipitating agent [33, 34]. Hereafter, the resulting catalyst is labelled as “fresh sample”. A reference gold catalyst supported on

carbon substrate (Au/C sample) was purchased from Premier Chemicals Limited, UK (NanAucat™ Gold Oxidation Catalyst).

Gold Cluster Characterization

A multi-technique approach was adopted to characterize the metal clusters sizes. To this aim, HERFD-XAFS spectroscopy was used in combination with scattering techniques, involving Small and Wide Angle X-ray Scattering (SAXS/WAXS), Scanning Electron Microscope (SEM) and Atomic/ Electrostatic Force Microscopy (AFM/EFM). This approach, as reported in literature, helps to overcome some drawbacks. Indeed, high resolution TEM potentially seems to be the key technique to calculate the particle size distribution for such materials. Nevertheless, the presence of aggregates or embedding phenomena, often occurring when highly dispersed metal clusters are deposited in a reducible oxide like the ceria, makes the determination of the particle borders quite hard and, sometimes also arbitrary. Moreover, it is well-known that metal particles smaller than or about 1 nm are hardly detected by standard TEM instruments, especially for ceria-supported gold catalyst where the electronic contrast is small. Finally, TEM analysis is carried out only on a small fraction of the entire metal particles population. For all these motivations, we focused our attention on SAXS and WAXS measurements which are a valid alternative to this purpose.[35-43] These techniques probe a larger volume of sampling which also assures a good statistic description of the system. For comparison reason, the shape of the clusters and their size by using AFM/EFM and SEM measurements were evaluated.

Small and Wide Angle X-Ray Scattering (SAXS/WAXS)

Simultaneous Small-angle X-ray scattering (SAXS) and wide-angle X-ray scattering (WAXS) experiments (X-ray wavelength λ= 1.001 Å), were carried out at the European Synchrotron Radiation Facility (ESRF), at DUBBLE

beamline (BM26B, Grenoble, France) [44]. SAXS data were reordered with a Pilatus 1M detector [45] positioned at a distance of 3.5 m from the sample holder (glass capillary). The WAXS patterns, were collected with a Pilatus 300K detector (1472 × 195 pixels of 172 μm × 172 μm) set at a distance of 2.00 m. The integration time for each simultaneous measurement was 30 s. The beam size was around 300 μm × 300 μm and its intensity on the sample was ~ 10^{11} photons/s. Data were subtracted from background contributions and normalized for synchrotron source intensity decay and X-ray transmission. $AgC_{22}H_{43}O_2$ (silver behenate) and α-Al_2O_3 (alumina) were used to calibrate the scattering vector q-scale, where $q = 4\pi\sin\theta/\lambda$ with θ being half of the scattering angle. An overview of the WAXS data is reported in Figure S1 and Figure S2 in the ESI file.

Atomic Force Microscopy (AFM) - Electrostatic force microscopy (EFM)

AFM measurements were carried out by using an AFM Cypher S from Asylum Research in the mode EFM. In order to measure the electrostatic behaviour of the sample, a Scout 70 RAu probe was used. The spring constant was 1.68N/m calculated from the thermal noise and the resonance frequency was around 60kHz. The value 0.02 Ωcm of the resistivity of the probe allowed to measure in EFM. A voltage of 3V was applied on the tip during EFM pass imaging. The full images are reported in Figure S3, Figure S4 and Figure S5 in the ESI file.

Scanning Electron Microscopy (SEM) - Energy Dispersive X-ray spectroscopy (EDX)

The SEM/EDX images were taken by a DSM 982 GEMINI with an EDX-detector silicon drift detector (ZEISS, Germany) at 10 kV (see Figure S6 in the ESI file). Spectra were acquired and analyzed by means of NSS 3.0 (Thermo Fisher Scientific, USA) program, probing the Ce-Lα (4.8403 KeV)

and Au Mα (4000 KeV).

X-ray photoelectron spectroscopy (XPS)

XPS analysis was performed by a VG Microtech ESCA 3000 Multilab spectrometer with Al K_α source ($h\nu$= 1486.6 eV). The binding energy scale (BE) was charge compensated using the C 1s peak (BE = 285.1 eV) from adventitious carbon. Curve fitting was performed with Voigt peak shape after Shirley background subtraction according to Sherwood [46]. Relative concentrations of chemical elements were calculated by a standard quantification routine, including Wagner's energy dependence of attenuation length [47] and a standard set of VG Escalab sensitivity factors. The uncertainty on the atomic quantitative analysis is about ± 10%. Assignment of photoelectron signals and peak components was determined according to literature reference database [48]. Results of XPS analysis are reported in Figure S7 in the ESI file.

CO adsorption tests

Adsorption and catalytic tests were performed in a pulse flow system using a Micromeritics AutoChem 2950 HP Chemisorption Analyzer, equipped with a thermal conductivity detector (TCD). The sample was introduced on a quartz wool in a quartz U-shaped tube used as reactor. Before adsorption of CO at room temperature, the 3% Au/CeO_2 and 1% Au/CeO_2 samples were pre-treated with a flowing gas mixture of 5% H_2 in Ar at atmospheric pressure for 1 h with a flow rate of 50 mL/min and the temperature of the catalyst bed was raised to 423 K at a rate of 10 K/min. Adsorption of CO at room temperature was realized by using a gas mixture of 1% of CO in He at a flux rate of 50 mL/min for 2 hrs. The catalytic CO oxidation with O_2 was registered as a function of the temperature in the range: 300 – 600 K. A reagent gas mixture of 1% of CO + 1% of O_2 in He over 35 mg of catalyst was used at a total flow

rate of 50 mL/min (STP), equivalent to a weight hourly space velocity (WHSV) of 42.000 mL g^{-1} h^{-1}. Before each gas switch, the reactor was purged with He for 5 min. The CO and CO_2 effluent gases were monitored via IR analyzers (ABB Uras 14).

In situ HERFD-XAFS

X-ray absorption spectroscopy measurements were carried out at the high-brilliance XAFS-XES beamline ID26 and at the Inelastic Scattering beamline ID20 of the European Synchrotron Radiation Facility (ESRF) in Grenoble, France [49, 50]. *In situ* and *ex situ* HERFD-XAFS measurements were performed at room temperature using the "microtomo reactor" available at ESRF.

The gas atmosphere in the reactor was controlled by three mass-flow controllers (Bronkhorst). The catalyst was exposed to different atmospheres as follows: pure He, 1% CO in He, and 20% O_2 in He (Air Liquide). The reactor exhaust was connected to a mass spectrometer (Pfeiffer QMS200) for monitoring the CO_2 formation during the HERFD-XANES evolution (see Figure S8 in ESI file). All HERFD-XANES measurements were performed *in situ* under a constant flux (20 mL min^{-1}) of gas through the reactor.

Each treatment cycle consisted of an exposure to CO and O_2 in succession, for 50 min and 30 min, respectively. Before each gas switch, the reactor was purged for 5 min with helium. The aerobic condition consisted of gas treatment by a mixture of 1% CO in He and 20% O_2 in He.

In order to avoid radiation damage, HERFD-XANES spectra were acquired every 10 s between 11900 and 12080 eV, with a continuous energy scan and in 200-380 different spots of the pelletized powder sample. For each measurement, different points of the pellet were scanned and then all the scans were summed up. For the *in situ* measurements, the spectra were recorded with the same energy step size and energy interval every 15 s. In

this case, 180 different spots were scanned on the sample in order to follow the structural kinetic for one hour. Full HERFD-EXAFS spectra, collected as the static XANES with an extended energy rage up to a 600 eV, were also measured under steady-state conditions. The spectra were also used to normalize the intensity of the HERFD-XANES data.

HERFD-EXAFS data analysis

HERFD-EXAFS spectra (two scans per sample) were energy-calibrated, averaged and then analyzed using GNXAS [51]. In this scheme, the local environment of the absorbing atom is divided into model atomic configurations containing 2, ..., *n* atoms (including the absorber). The theoretical EXAFS signal $\chi(k)$ is calculated by summing the *n*-body contributions γ^2, γ^3, ..., γ^n. For each configuration all the possible single and multiple scattering (MS) paths between the *n* atoms are considered.

Assuming a face-centered cubic (fcc) crystallographic arrangement for the gold clusters, two γ^2 *n*-body contributions are needed to calculate the first and second coordination shell, respectively. The first-shell Au−Au distance is connected to the fcc a-axis length by $R_1 = a/(2)^{1/2}$. The second neighbors are situated at R_2=a, where a is the gold lattice constant equal to 4.0782 Å. The higher shells are calculated by using selected three-body γ^3 contributions. The third-shell term at $R_3 = a(3)^{1/2}/2$ is modeled by considering an isosceles triangle with two first neighbors R_1 sides and vertex angle $\theta = 120°$. On the other hand, the fourth shell contribution R_4, involving the most intense multiple scattering contribution, is calculated from the degenerate ($\theta = 180°$) triangle formed by three aligned first neighbors corresponding to the diagonal of the cubic face.

The following parameters were released during the fitting procedure: the distance lattice parameter *a*; the Debye-Waller factor (σ^2); the angles of the γ^n contributions and the cluster size. In particular, the cluster dimension allows

to evaluate the reduction of coordination numbers in small particles, as indicated in the equation reported in literature.[52, 53] The equation, guessing a spherical form for the clusters, links the radius of the metal particles, the coordination number (CN) and distance R_i of the shells. [52, 53, 54, 29].
The $S0^2$ factor, the amplitude reduction term, was set at 0.9. The edge energy E_0 was set at 11919 eV and released during the minimization procedure.
The modeling of $\chi(k)$ to the experimental EXAFS signal allows to refine the structural parameters of the different coordination shells (see Figure S9 and S10 in the ESI file). The goodness of the structural model is also checked by comparing the experimental EXAFS signal Fourier transform (FT) with the FT of the calculated $\chi(k)$ function.

HERFD-XANES data analysis

HERFD-XANES spectra at the Au L3 edge were modelled by using the Finite Difference Method Near Edge Structure (FDMNES) software [55, 56]. The simulations were performed by using the multiple scattering theory based on the muffin-tin (MT) approximation for the potential shape of the Green theory. The MT radii were adjusted to have a good overlap between the different spherical potentials. A relativistic spin-orbit calculation was performed. In the calculation the Hedin-Lundqvist exchange potential was applied. The excitation of the absorbing atoms is taken into account by a core-hole accompanied by a screening charge set at their 5d level [55]. In order to model the variations in the average electronic occupancy on the metal particles during the reaction, semi-empirical *screening* was used and, accordingly, the value of this screening charge was used as a parameter [56]. In this respect, a set of Au L3 edge spectra corresponding to different values of *screening* were calculated. The calculated spectra were matched to the experimental data set for best agreement. This scheme of calculation was repeated for different clusters radii from 5 to 9 Å (see Figure S11 in ESI).

Results and discussion

Gold Cluster Characterization and CO adsorption tests.

Results of the cluster characterization are summarized in Figure 1 (see also Figure S1-S7 in the ESI file). Details of the analysis are reported in the ESI file.

As shown in Figure 1 (Panel A, II), the Scherrer analysis of the gold catalysts is not trivial. An unambiguously Lorentian peak at the (111) Bragg reflection relative to the fcc gold structure is evident in both XRD gold catalysts patterns. This highlights an important metal clusters poly-dispersion. The smartest way to analyze the data is to consider the (111) peak as the sum of a bimodal metal particles system. Accordingly, two different cluster sizes can be calculated. We found for both samples a larger contribution of small nanoparticles with an average size of 4 nm (approx. 70% in weight, see Table S1 in ESI file) and a minor population of bigger metal clusters (approx. 30% in weight, see Table S1 in ESI file) with an average size of approximately 10 nm. Although these latter particles are present in a small number but with a larger volume, they dominate in the XRD pattern. The SAXS analysis shown in Figure 1 (Panel B, I and II) allowed to calculated the size distribution function for each gold ceria and carbon supported catalyst. The details of the analysis are reported in the ESI file and the full results in Table S2. An average particle size of 1.5 and 1.4 nm for 1% and 3% Au/CeO_2 catalyst were obtained respectively. The mean metal particle size of gold supported on carbon is 1.7 nm.

The AFM/EFM analysis gives rise to a larger size distribution function, which gathers together the values achieved by SAXS, XRD and EXAFS (Figure 1, Panel D). It's worth noticing that larger grain dimension detected by AFM can be obtained by the aggregation of small metal clusters, whose size is obtained by SAXS or EXAFS (see Figure 1, Panel C). In fact, gold

nanoparticle aggregation during the deposition process takes place with a grainy morphology as observed in the AFM images in Figure 1. A deeper inspection of the Figure 1 shows that the grains are made up of individual gold metal clusters whose mean dimension is obtained by the SAXS analysis. Interestingly, SAXS and EXAFS analysis evidenced very similar average cluster size. On the other hand, SEM/EDX images shows a similar metallic distribution of larger aggregates on the ceria surface (see Figure S6 in ESI file).

The discrepancy of the results is not surprising. Since XRD is principally sensitive to the large crystallites, it is reasonable that dimension of the metal particles obtained with the XRD would be at or above the top end of the size interval found by SAXS and image techniques like AFM. In this respect, instead the EXAFS is on the bottom end of this range. [39, 44, 53, 54]. Accordingly, Scherrer analysis is not sensitive to the mean crystallite dimension, making SAXS and EXAFS an unique and valid alternative. In any case, the use of a multi-technique approach provides an indication of the degree of polydispersion that is present in the investigated system. Thus, the combination of such techniques allow to have a first evaluation of both size and polydispersion. Hence, from these measurements it is possible to conclude that: i) the cluster size of the 1% Au/CeO_2 and 3% Au/CeO_2 samples are similar; ii) no dramatic sintering effects are evident in the 3% Au/CeO_2 catalyst. These conclusions are summarized in Figure 1, Panel E.

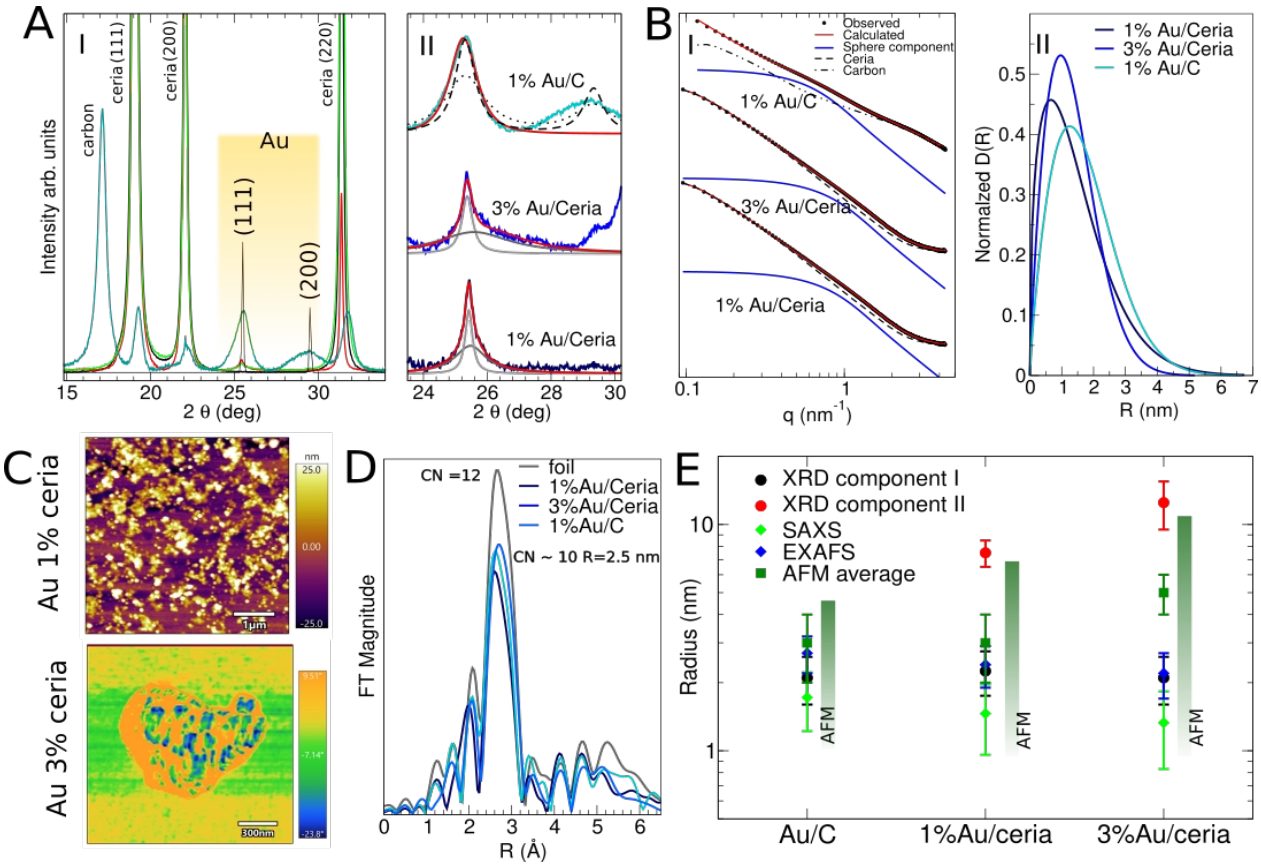

Figure 1. Panel A: I Overview of XRD patterns. II Scherrer analysis of the catalysts. The red line shows the fitting of the (111) peak. Grey lines show the different components used in the fitting. The dashed and the dot lines simulate XRD patterns for 4 nm and 8 nm gold metal clusters, respectively. Panel B: I Overview of SAXS analysis. II Distribution function obtained by the SAXS analysis. Panel C: AFM images for 1% Au/CeO_2 and 3% Au/CeO_2, respectively. Panel D: EXAFS signals compared with the Au foil. Panel E: Comparison of the metal cluster radius R in nanometer units obtained with different techniques.

CO adsorption at room temperature over 3%Au/CeO_2 and 1%Au/CeO_2 catalysts, after H_2 pre-treatment, is reported in Figure 2 (Left).

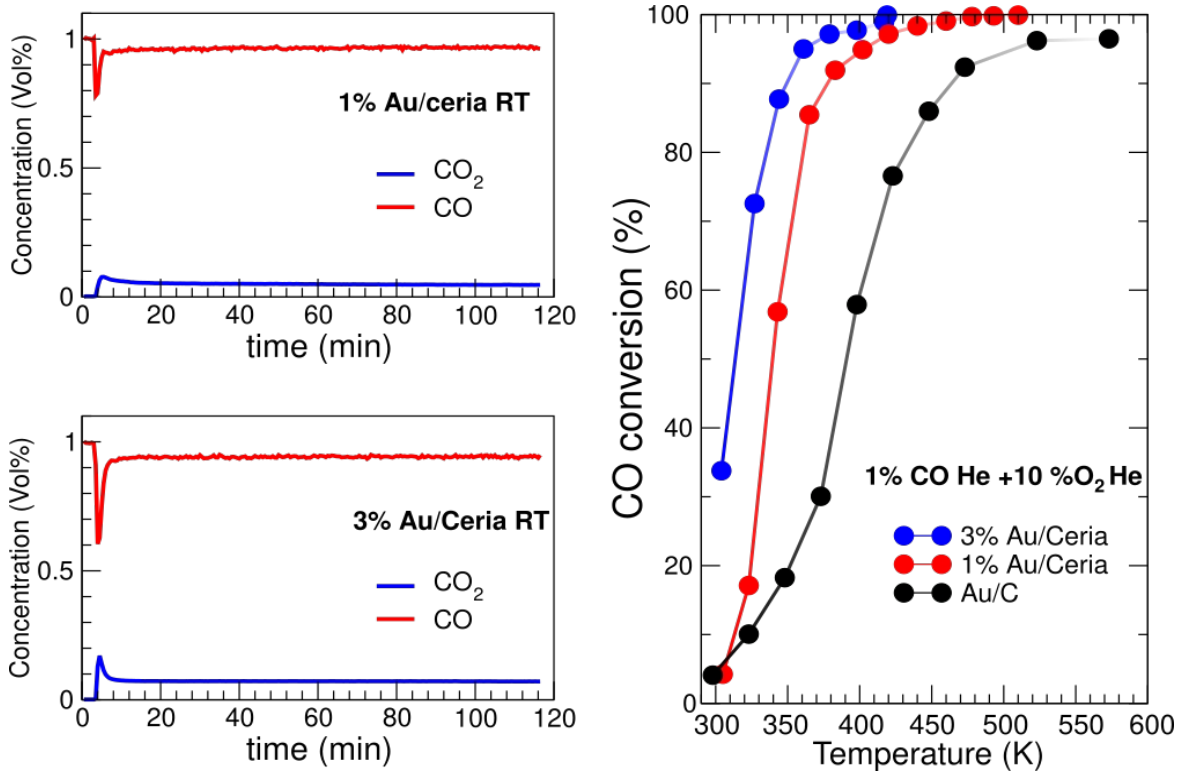

Figure 2. CO adsorption at room temperature over 1%Au/CeO_2 and 3%Au/CeO_2 catalysts, after H_2 treatment at 423K (Left). CO conversion (%) as a function of the temperature for the investigated catalysts (Right).

CO conversion into CO_2 occurs at room temperature on both the catalysts by means of the lattice oxygen from the ceria support. As expected, a higher production of CO_2 is detected on the 3%Au/CeO_2 with respect to the 1%Au/CeO_2 catalyst. The activity of the 3% Au/CeO_2 catalyst for CO oxidation as a function of the reaction temperature is shown in Figure 2 (Right). The temperature at which the CO conversion reached 50% (T_{50}) is taken as a measure of the catalytic activity. For the 3% Au/CeO_2 catalyst T_{50} corresponds to 313 K, thus confirming our previous results on the good catalytic performances of ceria-supported gold catalysts in the oxidation of CO [34].

Static HERFD-XANES

The XANES region of the X-ray absorption spectrum gives information about the density of states above the Fermi level. Figure 3 shows the static HERFD-XANES spectra of 3% Au catalysts, together with those of different gold references. In Panel **I** three main features: **a, b** and **c** of the experimental spectrum are highlighted. In particular, peak **a** is commonly known as the "white line", and it is due to $2p_{3/2} \rightarrow 5d_{5/2,3/2}$ transitions [20, 22, 23, 28, 29, 57, 58]. For metals with vacant *d*-orbitals this resonance is a sharp peak, and its intensity is directly correlated to the density of the unoccupied *d* states. This explains the very sharp "white line" in the gold(III) reference spectrum compared to the other spectra (see inset Figure 1), due to empty 5d states. The "white line" is in contrast quite suppressed both in the gold foil and in Au/C, as evidenced in Figure 3. On the other hand, a small peak is clearly visible in Au/CeO_2.

In the case of Au nanosized metal clusters, the 5*d* band is nominally full and, therefore, no resonance peak is expected. However, the hybridization of the 5*d* orbitals with the overlapping 6s and 6p orbitals determines an overall charge redistribution resulting in a small amount of 5d holes above the Fermi level [59, 60]. Moreover, the charge distribution and the relative occupancy, which is already altered by the cluster size, [13,19,23] can be affected by ligand binding and by interactions with the support [57-59]. Even in the absence of ionic gold, the presence of a resonance peak is an evidence for such an electronic perturbation, which increases the 5d-hole populations [59, 60]. It is important to notice that the "white line" cannot be modeled as the sum of ionic (Au^{3+} or Au^{+}) and Au^{0} components. In fact, results of the fitting of the spectra by using such component analysis indicate a fraction of Au cations of about 8-10% or 30-40%, depending on the cationic reference spectrum (Au^{3+} or Au^{+}) used in the analysis. This is contrast with the XPS results (see ESI file), that showed the presence of a very small ionic

contribution (Au^{+}) only on the surface of the 1% Au/CeO_2 catalyst. Au cations were not detected by XPS on the surface of 3% Au/CeO_2. In addition, such a component analysis can only be applied to a very limited energy range of the spectrum, in which the peak is present, and therefore lacks robustness (see Figure S11 and S12 in ESI file).

Accordingly, it can be inferred that the increased resonance peak mainly brings a contribution accountable to the metal support interaction [29, 58-61].

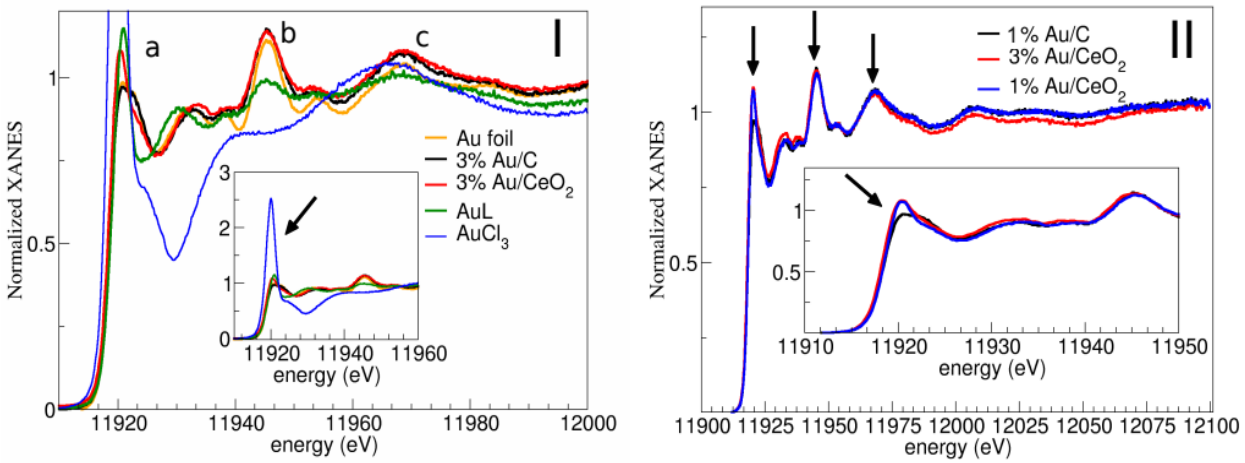

Figure 3. Panel I: XANES spectra of 1% Au/C (black), 3% Au/CeO_2 (red), Au foil (orange), gold(I) (dark green) [AuL,$(C_2H_5)_3PAuCl$] and $AuCl_3$ (blue). The main peaks are labelled as a, b and c. In the inset, the whole intensity of the Au^{3+} "white line" is compared to others. Panel II: Comparison of 3% Au/CeO_2 (red) with 1% Au/CeO_2 (blue) and Au/C sample (black). The arrows highlight the strong similarities between 1% and 3% Au/CeO_2.

The two peaks labelled **b** and **c** in Figure 3 yield information about the gold atomic arrangement. Remarkably, these peaks are diagnostic for the fcc atomic arrangement with more than two coordination shells and they are connected to the lattice parameter and the size of the metal gold clusters [57,58]. As the cluster size decreases, a shift towards higher energies and a broadening of the peaks occurs.

Irrespective of the different metal loading used, as showed in the previous paragraph, the metal clusters size is very similar for the two gold catalysts.

Hence the peaks **b** and **c**, characteristic of the fine structure, are nearly identical in height and in position (see Figure 3, Panel II).

In situ HERFD-XANES

In situ measurements were performed to follow the Au electronic state variations occurring during a redox cycle at 298 K, monitoring the resonance peak relative to 2p → 5d transition (peak **a**).

Results of the *in situ* measurements collected during the reducing treatment in CO are reported in Figure 4. After switching from inert gas to CO, an induction time of about 10 min is observed before reduction. An abrupt decrease of the resonance peak occurs upon reduction, about 10% of the normalized peak intensity.

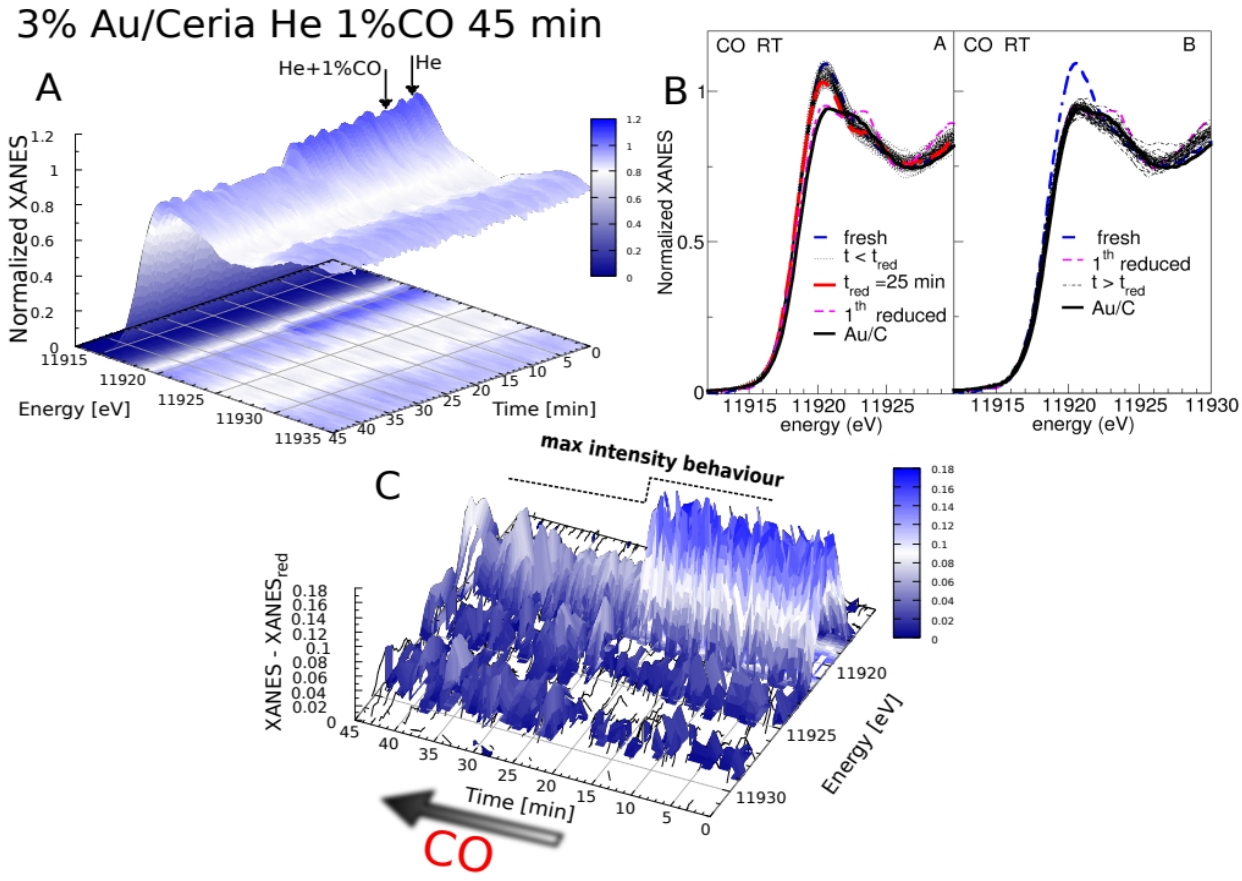

Figure 4. Panel A: Evolution of HERFD-XANES spectra of 3% Au/CeO_2 catalyst during the CO treatment. Panel B:-Superimposed XANES spectra, of

1%Au/CeO_2 and 1%Au/C during the CO reduction. For sake of clarity the kinetic has been split before and after the time t_{red} (indicated by the red line inside the graph) indicating the beginning of the reduction. Panel C: Relative intensity of the peak maximum minus the averaged reduced spectrum.

The reduction of the peak intensity is expected. CO reduces the ceria support inducing a strong modification of the oxide surface on which gold resides [62]. Ultimately, the metal-support interaction, arising from metal clusters with the surface oxygen bound with the support, is completely inhibited. The 5*d* band of gold is filled and then a decrease of the resonance peak is observed. No variation of the resonance peak was detected when the same reaction was performed using the Au catalyst deposited on carbon, as shown in Figure 5.

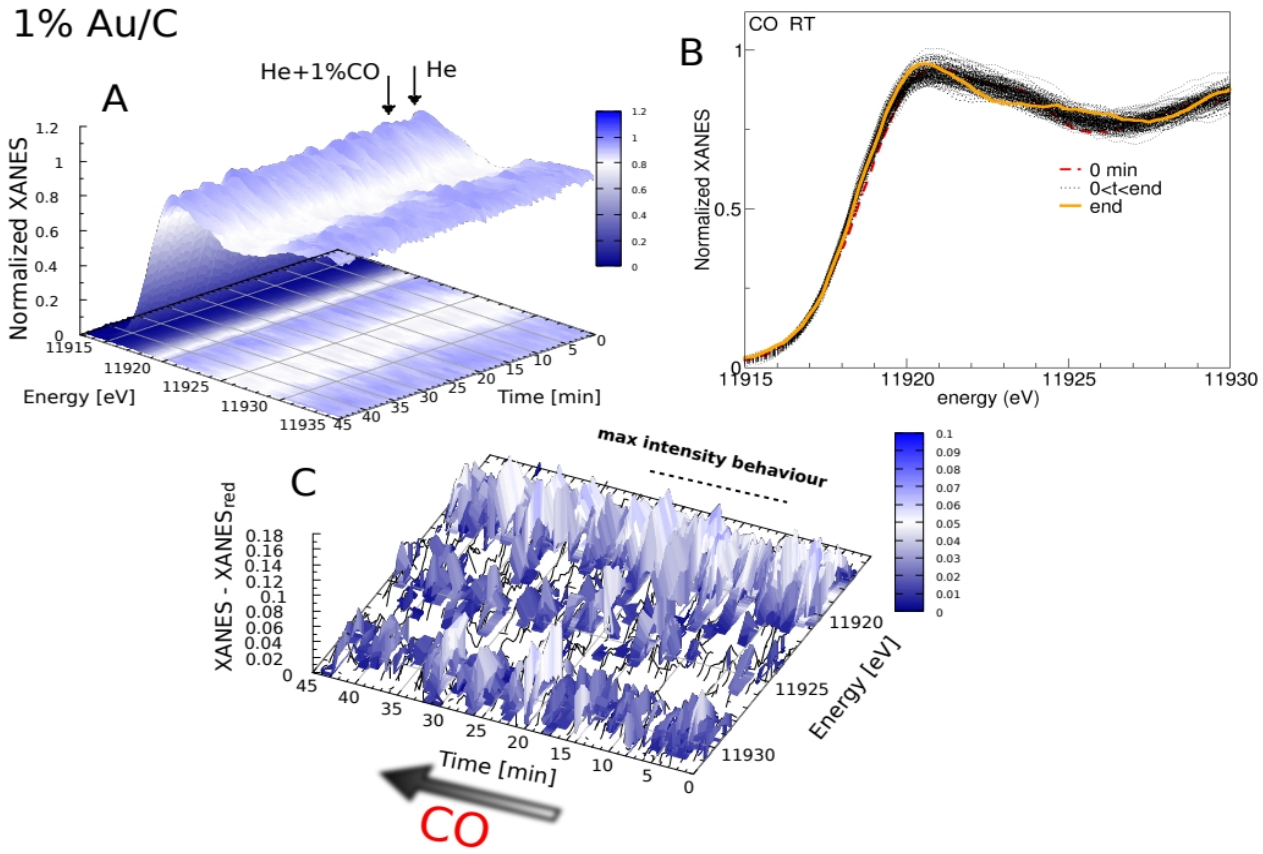

Figure 5. Panel A: Evolution of HERFD-XANES spectra of 1% Au/C catalyst during the CO treatment. Panel B: Superimposed XANES spectra. Panel C: Relative intensity of the peak maximum minus the averaged reduced spectrum.

Figure 6 shows a full redox cycle for the 3% Au/CeO_2 catalyst, performed

immediately after the exposure of the CO. After 5 min of oxygen treatment, an increase of the XANES resonance peak is detected. Then, the peak intensity starts fluctuating around an average value definitely higher than the fully reduced sample (1% Au/C) and lower than the fresh catalyst. Interestingly this behaviour, displaying an increase and decrease of the peak intensity, was observed during the whole oxidation process, as evidenced in Panels B and C of Figure 7. After switching to CO, a sharp lowering of the resonance peak was detected again.

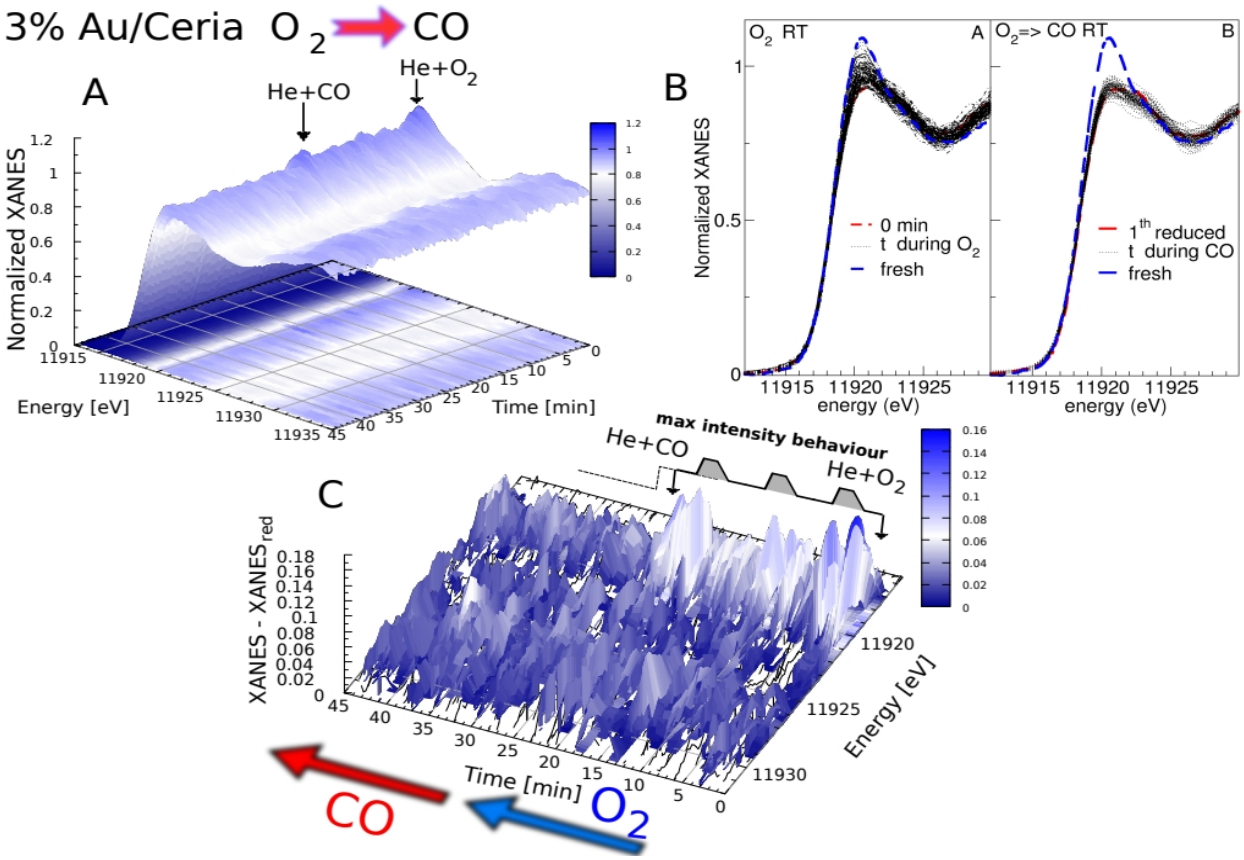

Figure 6. Panel A: Evolution of HERFD-XANES spectra of 3% Au/CeO_2 during the O_2/CO redox cycle. Panel B: XANES spectra. For sake of clarity the kinetic has been split before and after the time t_{red} (indicated by the red line inside the graph) in which the reduction starts. Panel C: Relative intensity of the peak maximum minus the averaged reduced spectrum.

The difference obtained in the two subsequent experiments is conclusive to distinguish a different *d*-band occupancy in reduced and oxidized state.

A similar trend was observed also for 1% Au/CeO_2, as summarized in Figure

7 and shown in Figures S14 and S15 in ESI file. In these plots, average *d*-band occupancy is probed via peak intensity, and three different values can be singled out and correlated to different redox conditions: fresh, reduced and oxidized. The comparison evidences that the peak intensity decrease is delayed by 20 min and the fluctuating behaviour is less evident in 1% Au/CeO_2. All considered, the average *d*-band occupancy is similar to that obtained for 3% Au/CeO_2, as shown in Figure 6.

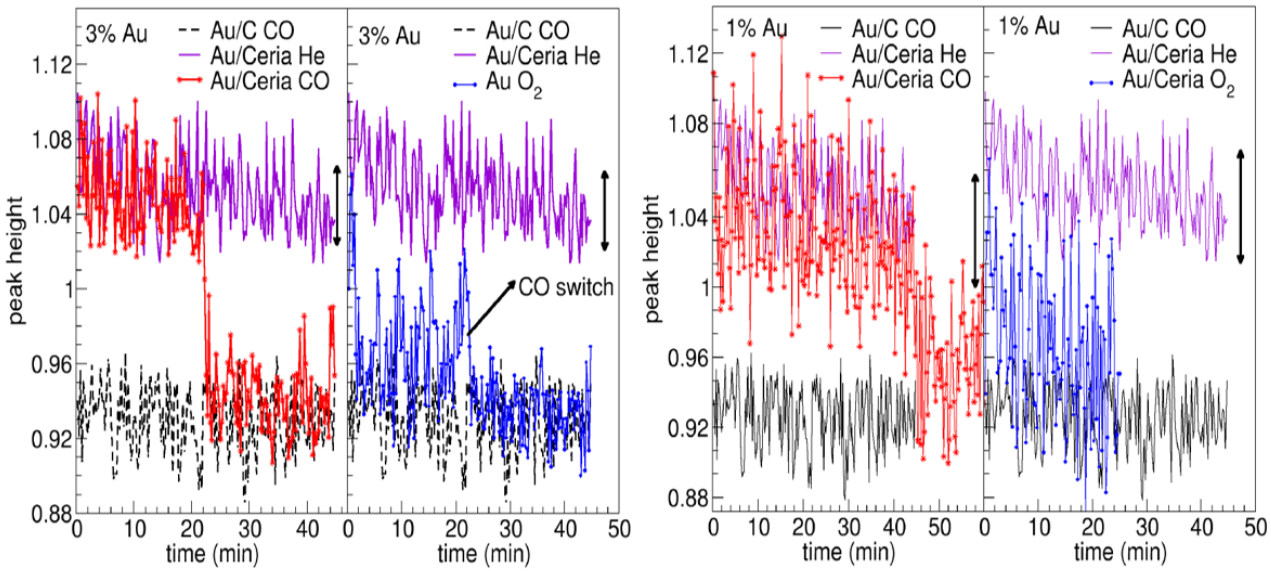

Figure 7. Time-resolved peak intensity for 3% Au/CeO_2 (left panel) and 1% Au/CeO_2 (right panel) for the redox treatments in constant flux (20 mL min^{-1}) of gas (He/CO or He/O_2) The arrows indicate the fluctuation of the maximum value of the "white line" (approx. ±0.02 and ±0.03, respectively). Au/C is shown for comparison.

A further fresh 3% Au/CeO_2 sample was exposed to a CO/O_2 mixture (Figure 8) and a continuous decrease of the resonance peak was observed. Interestingly, after 25 min, the resonance peak reached a constant trend, whose average value matches the one obtained in the re-oxidation reaction of the reduced sample. This value lies between those obtained for the fresh and the fully reduced catalyst. This result, compared with those achieved in the other cycles, is summarized in Figure 9.

The difference kinetic behavior of the two different loaded Au catalysts

reported in Figure 7, can be explained considering the different number of metallic active sites which, in first approximations, can be directly correlated with the different metallic load of the two catalysts.

This observation is supported by a more thorough comparison of the size distribution functions, (see figure 1 panel B and E and in table S1 of the ESI file) which highlghts that the 3% weight Au catalyst have a definitively higher number of small metal gold clusters and then more reactive sites.

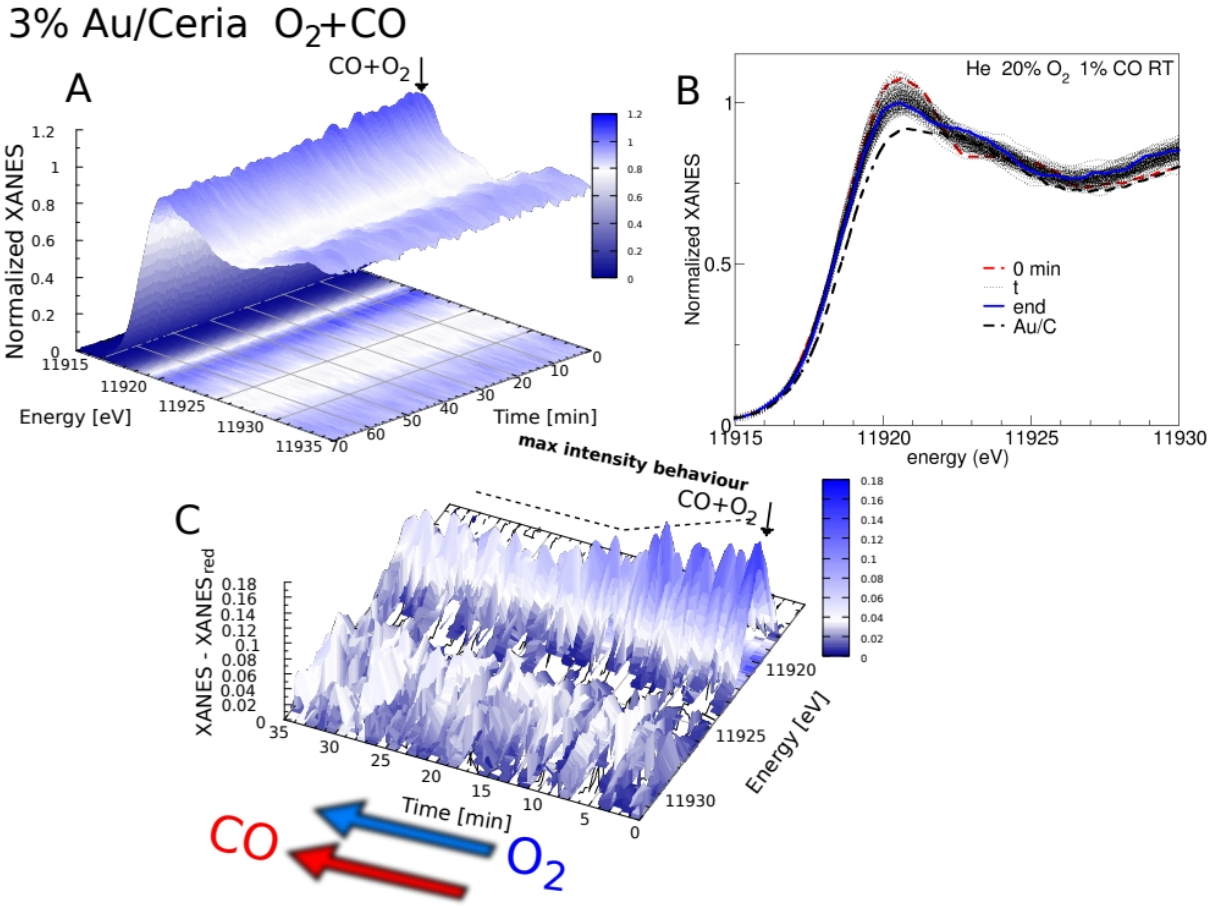

Figure 8. Panel A: Evolution of HERFD-XANES spectra of 3% Au/CeO_2 during the O_2+CO mixture treatment. Panel B: XANES spectra. Panel C: Relative intensity of the peak maximum minus the averaged reduced spectrum.

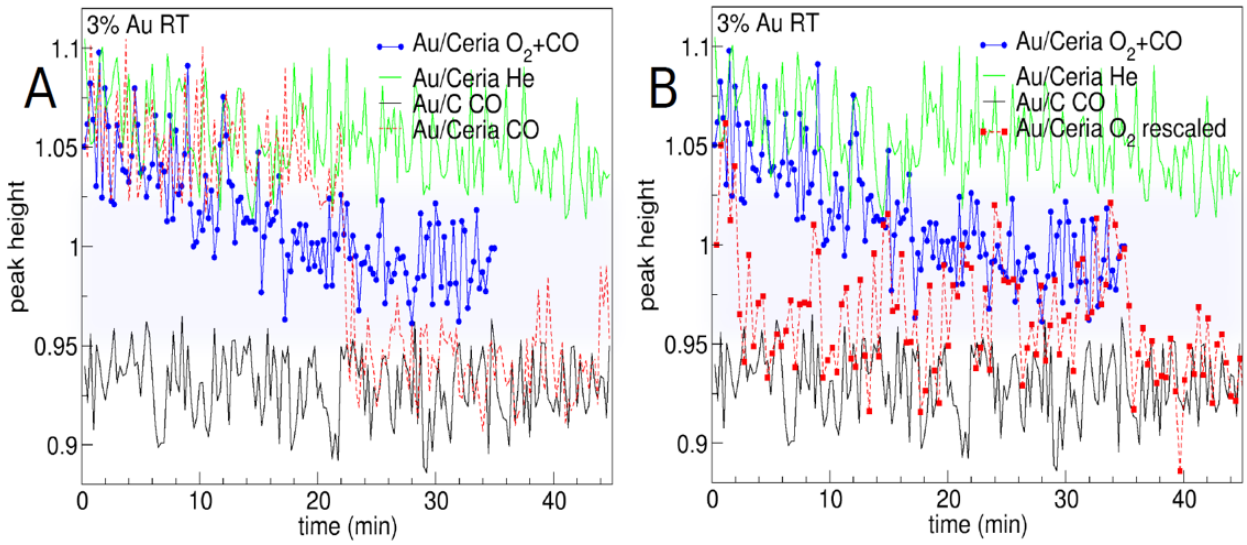

Figure 9. Time-resolved peak intensity of 3% Au/CeO_2 during different treatments. Panel A: Comparison of the $CO+O_2$ mixture with respect to CO reduction. Panel B: Comparison of the $CO+O_2$ gas mixture with respect to O_2 oxidation. The results measured in O_2 were time-shifted for better comparison. Results of Au/C reduction in CO are reported as a reference.

XANES modeling and discussion

As expected, the reaction mechanism of CO oxidation is different in the aerobic and anaerobic conditions. In anaerobic conditions, an abrupt change of *d*-band occupancies correlated with the sudden change of the resonance peak is observed after an induction period. CO conversion starts as soon as the CO/He mixture is in contact with the catalyst, as witnessed by the mass quadrupole signal analyzing the reactor exhaust. The CO oxidation occurs by consuming the oxygen atoms, either adsorbed or in the lattice. The latter process leads to the reduction of surface or subsurface Ce(IV) species, and it does not result in any modification of the metal gold clusters [62, 16, 22]. After the oxygen depletion of the support surface layer, bulk reduction takes place and the metal clusters are fully reduced loosing their interaction with the support as well [61].

During the CO oxidation in anaerobic condition, most oxygen atoms are

provided by the ceria support, which, consequently, will results strongly defective at the end. When the re-oxidation of the sample starts, molecular oxygen is first bound on the metal cluster surface. Therefore, the 5*d* band occupancy decreases, and a corresponding increase of the resonance peak is detected. In this step, molecular oxygen is activated and it can be conveyed to the ceria lattice in order to refill the O^{2-} vacancies in the support [63]. The transfer of activated oxygen to the oxide, breaking the Au-O bond, corresponds to an increase of the gold 5*d* band occupancy, with the consequent lowering of the resonance peak (see Figure 4). It can be argued that, during the oxygen migration in the ceria lattice, an induction is needed before the metal can adsorb O_2 again. During this time, the gold cluster keeps the 5*d* band full, so no relevant change of the resonance peak is observed. The acquisition time used for the *in situ* measurements (10 s) is definitely slower than the turnover of oxygen reduction. Therefore, the time averaging of the sample in different d-band occupancies could explain the irregular fluctuating behavior.

A different scenario occurs when CO oxidation takes place in the presence of oxygen (aerobic conditions). In this case, molecular oxygen adsorbed on the metal surface or in contact with the Au cluster is activated and reacts directly with CO [63]. Due to the simultaneous process of emptying and filling the Au 5*d* band, an average occupancy value is reached, which results in a smooth variation of the resonance peak. The gradual decrease of the “white line” lasts around 15 min before reaching the eventual average value (see Figure 7): therefore, an initial structural rearrangement of the metal clusters and the formation of active gold-oxides species must be taken into account [13,15-16, 22, 28, 63-65].

In order to validate the hypothesis that the variation of resonance peak upon the different chemical treatments can be ascribed mainly by the partial depletion of the d-band occupancy, the XANES spectra were simulated from

first principles with the FDMNES package (Figure 8).

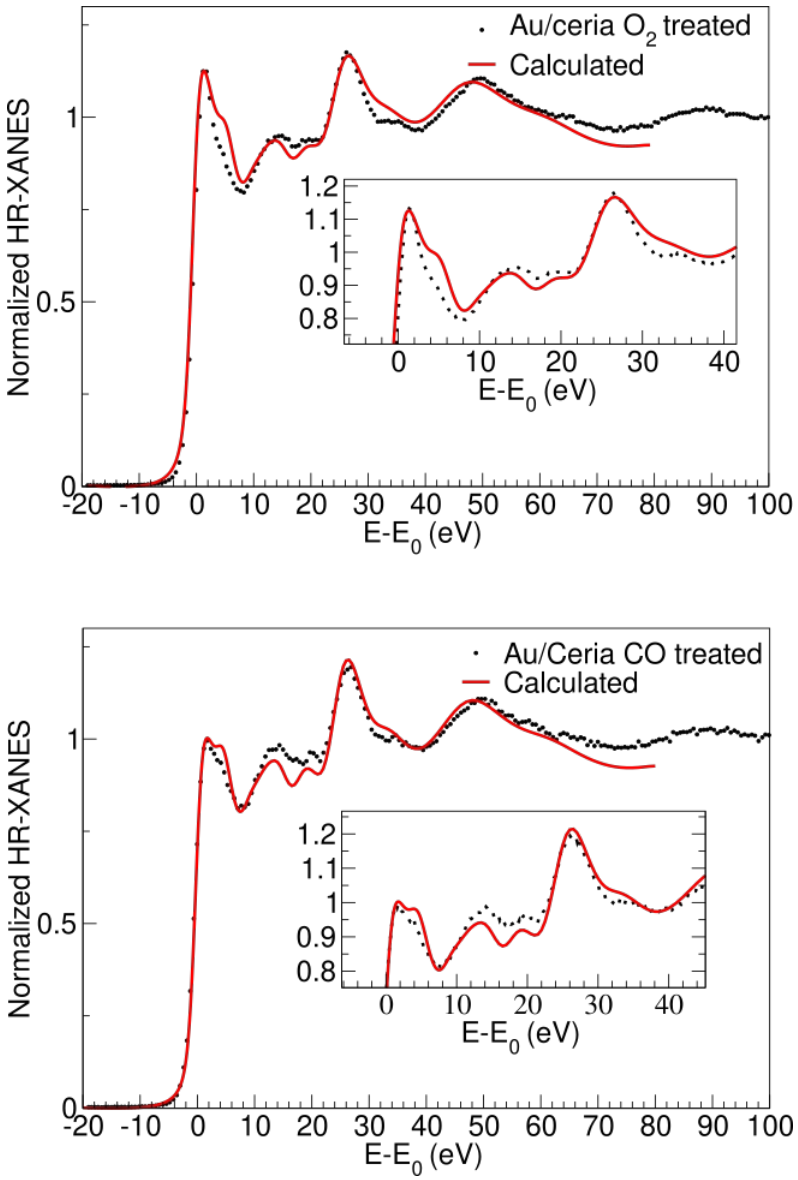

Figure 10. HERFD-XANES spectra and simulations of 3% Au/CeO_2. Panel A: Observed spectrum reduced in CO (black), and model (red). Panel B: Observed spectrum re-oxidized in O_2 (black), and model (red)

The key parameter to reproduce the variable 5d band occupancy is the semi-empirical correction term *screening*. By changing the screening parameter, the electronic charge in the unfilled valence orbital of the absorber is modified resulting in an additional electron in the first unoccupied state, while the

absorbing atom maintains its (almost) neutral state.[55, 66] The screening parameter in principle range from 0 (no screening charge, absorbing atom is formally close to 1+) to 1 (full screening, absorbing atom is almost neutral).

Within the energy range of interest, all main features of the Au L3 edge are well reproduced by using a *screening* values of 0.9 for reduced catalyst. For the fresh and re-oxidized catalyst *screening* was kept at the default value of one, representing the fully removed core electron. The evidence that the positive core-hole charge is not fully screened (only 0.1 charge missing in the unoccupied level) suggests a correlation effect caused by the presence of the excited 5*d* electron that hinders the screening process [55], which corroborates the possible interaction of the metal cluster either with the ceria support or the adsorbed oxygen molecules. In any case this produces a depletion of the electronic occupancy of the d band as highlighted by the calculations. Moreover, it can be argued that since the spectra are collected in high resolution mode, a similar variation observed in the resonance peak should be also expected in fine structure 20-40 eV above the edge. In fact, due to the changing of the electronic structure, as evidenced in the standards [67], the formation of either Au^{3+} or Au^{1+} should induce a visible broadening or a reduction of the peaks intensity. However, this is not observed and the variation is mainly limited at the resonance peak. So the reported variation is interpreted as a partial positive charge of the gold cluster corresponding to a small lower shift the Fermi level whit subsequent partial depletion of the states. Moreover, considering that any energy shift position is produced in the calculation even if not detected in the experimental data, we excluded a full oxidation process.

Notably, the metal cluster radius considered in the model is 9 Å, which is the best size to reproduce the shape of the resonance peak and the fine structure above the edge (see Figure S11 in ESI file). In addition, no cationic species were considered in the calculation showed in Figure 8.

The increase of the resonance peak in gold ceria catalyst after exposure to oxygen is not fully surprising and it has been already reported in the literature [16, 22, 26]. However, it is worth noting that the current calculations here reported suggest that the increase of the resonance is not related to the oxidation of the gold clusters but rather to a depletion of the metallic band which indicates a partial positive charging of the clusters.

In comprehensive studies, it was already reported that ionic gold is not participating in the oxidation of CO [16, 26]. In addition, it was also suggested that the small gold clusters are the only active species, so that the catalytic activity is related to bridged surface groups adsorbed on interfacial Au atoms of these small particles which, for instance, in the case of water shift gas reaction are the OH groups [16]. In contrast with the reported results [14, 16, 26], which were obtained with conventional XAS, our findings prove the existence of partially charged metal clusters that originate from a temporarily depleted gold 5d band during the oxidation reaction. This results are also corroborated by combined DFT calculations with a genetic algorithm (GA) and a biased grand canonical Monte-Carlo (b-GCMC) approach, which prove the role of positively charged gold atoms in CO oxidation in supported and highly dispersed Au/CeO_2 catalysts [68].

Moreover, these results support the possible mechanism of CO oxidation over Au/CeO_2 catalyst which involves the adsorption of molecular oxygen onto defect sites located at the gold–ceria peripheral interface. In particular, according to the Mars–van Krevelen (MvK) mechanism, the oxygen vacancies in proximity of the $Au\text{-}CeO_2$ interface are the potential anchoring sites for O_2 that subsequently reacts with Au–CO to form CO_2. In this case the the partially positive gold cluster (see Figure 9) could have a key role helping the interaction between the molecular oxygen and the ceria. If needed, also the oxygen from the lattice can be consumed by the reaction with CO. This process again will produce oxygen vacancies. The formed oxygen vacancies

can be refilled by diffusion of peroxide species from the vicinity of the gold–ceria interface perimeter. Again in this step, the positive partially charged state of the metal cluster might have a crucial role in the stabilization of the gold–ceria-peroxide complex.[63, 68]

Conclusions

Nanosized gold catalysts supported on ceria were investigated by *in situ* HERFD-XAFS at the Au L3-edge during treatments with O_2 and CO. Time-resolved measurements revealed the active role of 5d orbitals from Au metal during the CO oxidation. Experimental data evidenced that the occupancy of the 5d band is a reversible process occurring when reductive or oxidizing conditions are switched. A fluctuating behavior of the XANES resonance peak was evidenced during the O_2 treatment and this can be related to the variation of the population of 5*d* band during the oxidation process. The results are corroborated by extensive *ab initio* simulations, showing that the change in “white line” intensity is related to a modification of the occupation of the gold 5d band via changes in the core-hole screening.

AUTHOR INFORMATION

Corresponding Author

* Alessandro Longo, alessandro.longo@esrf.fr

* Maria Pia Casaletto, mariapia.casaletto@cnr.it

Author Contributions

The manuscript was written through contributions of all authors.

Funding Sources

CNR-ISMN is acknowledged for the financial support for the materials used in the synthesis of the catalysts.

Notes

The authors declare no competing financial interest.

ASSOCIATED CONTENT

Supporting Information.

Additional experimental results of surface and bulk analysis by XPS, XRD, AFM, SEM-EDS, EXAFS and data processing. This material is available free of charge via the Internet at http://pubs.acs.org.

ACKNOWLEDGMENTS

Support from the European Synchrotron Radiation Facility (ESRF) Grenoble, France, is grateful acknowledged. The authors thank the PSCM platform (Grenoble) for access to the AFM laboratories, Dr. Marie Capron for AFM and EFM measurements and Dr. Diego Pontoni for technical support. We gratefully acknowledge G. Pantaleo (CNR), and G. Raimondi (MPI-FKF) for technical support and data acquisition.

REFERENCES

[1] Haruta, M.; Kobayashi, T.; Sano, H.; Yamada, N.; Novel Gold Catalysts for the Oxidation of Carbon Monoxide at a Temperature far below 0º C. *Chem. Lett.* **1987**, 405-408.

[2] Liu, X.; Liu, M.H.; Chia Luo, Y. C.; Mou, C.Y.; Lin, S.D.; Cheng, H.; Chen, J.M.; Lee, J.F.; Lin, T.S.; Strong Metal–Support Interactions between Gold Nanoparticles and ZnO Nanorods in CO Oxidation. *J. Am. Chem. Soc.* **2012**, 134, 10251−10258.

[3] Liu, Y.; Jia, C. J.; Yamasaki, J.; Terasaki, O.; Schüth, F.; *Angew.* Highly Active Iron Oxide Supported Gold Catalysts for CO Oxidation: How Small

Must the Gold Nanoparticles Be? *Chem., Int. Ed.* **2010**, 49, 5771-5775.

[4] Valden, M.; Lai, X.; Goodman, D. W.; Onset of Catalytic Activity of Gold Clusters on Titania with the Appearance of Nonmetallic Properties. *Science* **1998**, 281,1647–1650.

[5] Herzing, A. A.; Kiely, C. J.; Carley, A. F.; Landon, P.; Hutchings,G. J.; Identification of Active Gold Nanoclusters on Iron Oxide Supports for CO Oxidation. *Science* **2008**, 321, 1331–1335.

[6] Carrettin, S.; Concepciòn, P.; Corma, A.; López Nieto, J. M.; Puntes, V. F.; Nanocrystalline CeO_2 Increases the Activity of Au for CO Oxidation by Two Orders of Magnitude. *Angew. Chem. Int. Ed.* **2004**, 43, 2538–2540.

[7] Si, R.; Flytzani-Stephanopoulos, M.; Shape and Crystal-Plane Effects of Nanoscale Ceria on the Activity of Au-CeO_2 Catalysts for the Water–Gas Shift Reaction. *Angew. Chem. Int. Ed.*, **2008**, 47*,* 2884–2887.

[8] Widmann, D.; Behm, R. J.; Activation of Molecular Oxygen and the Nature of the Active Oxygen species for CO Oxidation on Oxide Supported Au Catalysts. *Acc. Chem. Res.* **2014**, 47, 740–749.

[9] Widmann, D.; Behm, R. J.; Active oxygen on a Au/TiO_2 Catalyst: Formation, Stability, and CO Oxidation Activity. *Angew. Chem. Int. Ed.* **2011**, 50, 10241–10245.

[10] Fu, Q.; Saltsburg, H.; Flytzani-Stephanopoulos, M.; Active nonmetallic Au and Pt species on ceria-based water-gas shift catalysts. *Science* **2003**, 301, 935–938.

[11] López-Haro, M.; Cíes, J. M.; Trasobares, S.; A Pérez-Omil, J.; Delgado, Juan J.; Bernal, S.; Bayle-Guillemaud, P.; Stéphan, O.; Yoshida, K.; Boyes, E. D.; Gai, P. L.; Calvino, J.J.; . Imaging Nanostructural Modifications Induced by Electronic Metal-Support Interaction Effects at Au Parallel to Cerium-Based Oxide Nanointerfaces. *ACS Nano* **2012**, 6, 6812–6820.

[12] Kumar, G.; Tibbitts, L.; Newell, J.; Panthi, B.; Mukhopadhyay, A.; Rioux, R. M.; Pursell, C. J.; Janik M.; and Chandler, B. D.; Evaluating Differences in

the Active-Site Electronics of Supported Au Nanoparticle Catalysts Using Hammett and DFT Studies. *Nat. Chem.* **2018,**10, 268–274.

[13] Wang, Y. G.; Mei, D.; Glezakou, V.-A.; Li, J.; Rousseau, R.; Dynamic Formation of Single-Stom Satalytic Sctive Sites on Seria-Supported Gold Nanoparticles. *Nat. Commun.* **2015**, 6, 6511-6519.

[14] Guo,L. W.; Du, P.-P.; Fu, X. P.; Ma, C.; Zeng, J.; Si, R.; Huang, ; Y.-Y.; Jia, C. J.; Zhang, Y.-W.; Yan, C.-H.; Contributions of Distinct Gold Species to Catalytic Reactivity for Carbon Monoxide Oxidation, *Nat. Commun*, **2016**, 7, 13481-13489

[15] Hea, Y.; Liu, J. C.; Luod, L.; Wang, Y.-G.; Zhue, J.; Dug, Y.; Li, J.; Maoa, S. X.; Wang, C.; Size-Dependent Dynamic Structures of Supported Gold Nanoparticles in CO Oxidation Reaction Condition, *PNAS*, **2018**, vol. 115, 30, 7700–7705.

[16] Fu,X. P.; Guo, L.-W.; Wang, W.-W.; Ma, C.; Jia, C J.; Wu, K.; Si, R.; Sun, L. D.; Yan, C. H.; Direct Identification of Active Surface Species for the Water−Gas Shift Reaction on a Gold−Ceria Catalyst, *J. Am. Chem. Soc.* **2019**, 141, 4613−4623.

[17] Hakkinen, H.; Abbet, S.; Sanchez, A.; Heiz, U.; Landman, U.; Structural, Electronic, and Impurity-Doping Effects in Nanoscale Chemistry: Supported Gold Nanoclusters, *Angew. Chem. Int. Ed.* **2003**, 42, 11, 1297-1300.

[18] Yoon, B.; Hakkinen, H.; Landman, U.; Worz, A. S.; Antonietti, J.-M.; Abbet, S.; Judai, K.; Heiz, U.; Charging Effects on Bonding and Catalyzed Oxidation of CO on Au8 Clusters on MgO, *Science* **2005**, 307, 21, 403-407.

[19] Hammer, B.; Norskov J. K.; Why Gold Is the Noblest of All the Metals. *Nature* **1995**, 376, pages238–240.

[20] van Bokhoven, J. A.; Louis, C.; Miller, J. T.; Tromp, M.; Safonova, O. V.; Glatzel, P.; Activation of Oxygen on Gold/Alumina Catalysts: In Situ High-Energy-Resolution Fluorescence and Time-Resolved X-ray Spectroscopy, *Angew. Chem. Int. Ed.* **2006**, 118, 4767–4770.

[21] Glatzel, P.; Singh, J.; Kvashnina, K. O.; van Bokhoven, J. A.; In situ Characterization of the 5d Density of States of Pt Nanoparticles Upon Adsorption of CO. *J. Am. Chem. Soc.* **2010**, 132, 2555–2557.

[22] Weiher, N.; Beesley, A. M.; Tsapatsaris, N.; Delannoy, L.; Louis, C.; van Bokhoven, J. A.; Schroeder, S. L. M.; Activation of Oxygen by Metallic Gold in Au/TiO2 Catalysts, *J. Am. Chem. Soc*. **2007**, 129, 2240-2241.

[23] Visikovskiy, A.; Matsumoto, H.; Mitsuhara, K.; Nakada, T.; Akita, T.; Kido, Y.; Electronic d-Band properties of Gold Nanoclusters Grown on Amorphous Carbon. *Phys. Rev. B.* **2011**, 83,16, 165428-165437.

[24] Tian, C.; Zhang, H.; Zhu, X.; Lin, B.; Liu, X.; Chen, H.; Zhang, Y.; Mullins, D. R.; Abney, C. W.; Shakouri, M.; Chernikov, R.; Hu, Y.; Polo-Garzon, F.; Wu, Z.; Fung, V.; Jiang, D.; Liu, X.; Chi, M.; Liu, J.; Dai, S.; A New Trick for an Old Support: Stabilizing Gold Single Atoms on $LaFeO_3$ Perovskite. *Appl. Catal. B Environ.*, **2020**, 261, 118178.

[25] Corma, A.; Concepción, P.; Boronat, M.; Sabater, M. J.; Navas, J.; Yacaman, M. J.; Larios, E.; Posadas, A.; López-Quintela, M. A.; Buceta, D.; Mendoza, E.; Guilera G.; and Mayoral, A.; Exceptional Oxidation Activity with Size-Controlled Supported Gold Clusters of Low Atomicity. *Nat. Chem.* **2013**, 5, 775-781.

[26] Abdel-Mageed, A. M.; Kučerová, G.; Bansmann, J.; and Behm,R. J.; Active Au Species During the Low-Temperature Water Gas Shift Reaction on Au/CeO2: A Time-Resolved Operando XAS and DRIFTS Study. *ACS Catal.* **2017**, 7, 6471−6484.

[27] Pacchioni, G.; Electronic Interactions and Charge Transfers of metal Atoms and Clusters on Oxide Surface. *Phys*. *Chem. Chem Phys.* **2013**, 15, 1737-1757.

[28] Miller, J .T.; Kropf, A. J.; Zha, Y.; Regalbuto, J.R.; Delannoy, L.; Louis, C.; Bus, E.; van Bokhoven, J.A.; The Effect of Gold Particle Size on the Au-Au Bond Distance in Supported Catalysts. *J. Catal.* **2006**, 240, 222-234.

[29] Longo, A.; Liotta, L.F.; Pantaleo, G.; Giannici, F.; Venezia, A.M.; Martorana, A.; Structure of the Metal–Support Interface and Oxidation State of Gold Nanoparticles Supported on Ceria. *J. Phys. Chem. C* **2012**, 16, 2960−2966.

[30] Singh, J.; Tromp, M.; Safonova, O. V.; Glatzel, P.; van Bokhoven, J. A.; In Situ XAS with High-Energy Resolution: The Changing Structure of Platinum During the Oxidation of Carbon Monoxide *Catal. Today* **2009**, 145, 300–306.

[31] Hoffman, A. S.; Sokaras, D.; Zhang, S.; Debefve, L. M.; Fang, C. Y.; Gallo, A.; Kroll, T.; Dixon, D. A.; Bare, S. R.; Gates, B. C.; High-Energy-Resolution X-ray Absorption Spectroscopy for Identification of Reactive Surface Species on Supported Single-Site Iridium Catalysts. *Chem. Eur. J.* **2017**, 23, 14760-14768.

[32] Bunau, O.; Joly, Y.; Self-Consistent Aspects of X-ray Absorption Calculations. *J. Phys.: Condens. Matter* **2009**, 21, 345501-345512.

[33] Casaletto, M. P.; Longo, A.; Venezia, A.M.; Martorana, A.; Prestianni, A.; Metal-Support and Preparation Influence on the Structural and Electronic Properties of Gold Catalysts. *Appl. Catal. A: General* **2006***,* 302, 309–316.

[34] Venezia, A. M.; Pantaleo, G.; Longo, A.; Di Carlo, G.; Casaletto, M.P.; Liotta, L.F.; Deganello, G.; Relationship Between Structure and CO Oxidation Activity of Ceria-Supported Gold Catalysts. *J. Phys. Chem. B* **2005**, *109,* 2821-2827.

[35] Pabisch, S.; Feichtenschlager, B.; Kickelbick, G.; Peterlik, H.; Effect of interparticle interactions on size determination of zirconia and silica based systems - A comparison of SAXS, DLS, BET, XRD and TEM. *Chem. Phys. Lett.* **2012**, 521, 91–97.

[36] Rumancev, C.; von Gundlach, A. R.; Baier, S.; Wittstock, A.; Shi, J.; Benzi, F.; Senkbeil,T.; Stuhr, S.; Garamusx, V. M.; Grunwaldt, J. D.;

Rosenhahn, A.; Morphological analysis of cerium oxide stabilized nanoporous

gold catalysts by soft X-ray ASAXS. *RSC Adv.*, **2017**, 7, 45344.

[37] Wilcoxon, J. P.; Abrams, B. L.; Synthesis, structure and properties of metal nanoclusters. *Chem. Soc. Rev.*, **2006**, 35, 1162–1194.

[38] Koerner, H.; MacCuspie, R. I.; Park, K.; and Vaia, R. A.; In Situ UV/Vis, SAXS, and TEM Study of Single-Phase Gold Nanoparticle Growth. *Chem. Mater.* **2012**, 24, 6, 981–995

[39] Agostini, G.; Lamberti, C.; Pellegrini, R.; Leofanti, G.; Giannici, F.; Longo, A.; and Groppo, E.; Effect of Pre-Reduction on the Properties and the Catalytic Activity of Pd/Carbon Catalysts: A Comparison with Pd/Al2O3. *ACS Catal.* **2014**, 4, 187−194.

[40] Jensen, H.; Pedersen, J. H.; Jørgensen, J. E.; Pedersen, J. S.; Joensen, K. D.; Iversen, S. B.; Søgaard, E. G.; *J. Exp. Nanosci.* **2006**, 1:3, 355-373.

[41] Harada, M.; Tamura, N.; Takenaka, M.; Nucleation and Growth of Metal Nanoparticles during Photoreduction Using In Situ Time-Resolved SAXS Analysis. *Phys. Chem.* C **2011**, 115, 14081–14092.

[42] L.F. Liotta, L. F.; Longo, A.; Macaluso, A.; Martorana, A.; Pantaleo, G.; Venezia, A.M.; Deganello, G.; Influence of the SMSI effect on the catalytic activity of a Pt(1%)/$Ce_{0.6}Zr_{0.4}O_2$ catalyst: SAXS, XRD, XPS and TPR investigations. *Appl. Catal. B*: *Environmental*, **2004**, 48, 2,18,133-149.

[43] Longo, A.; Martorana, A.; *J. Appl. Crystallogr.* **2008** 41, 446-455.

[44] Portale, G.; Cavallo, D.; Alfonso, G.C.; Hermida-Merino, D.; van Drongelen, M.; Balzano, L.; Peters, G.; Goossens, J.; Bras, W.; Polymer Crystallization Studies under Processing-Relevant Conditions at the SAXS/WAXS DUBBLE Beamline at the ESRF. *J. Appl. Crystallogr.* ***2013***, 46, 1681–1689.

[45] Henrich, B.; Bergamaschi, A.; Broennimann, C.; Dinapoli, R.; Eikenberry, E.F.; Johnson, I.; Kobas, M.; Kraft, P.; Mozzanica, A.; Schmitt, B. PILATUS: A Single Photon Counting Pixel Detector for X-Ray Applications. *Nucl. Instrum. Methods Phys. Res.* **2009**, 607, 247–249.

[46] Sherwood, P. M. A.; Briggs, D.; Seah, M. P.; Data Analysis in X-ray Photoelectron Spectroscopy in Practical Surface Analysis by Auger and X-ray Photoelectron Spectroscopy. Wiley, New York **1990**, 1

[47] Wagner, C. D.; Davis L. E. and Riggs, W.M.; The Energy Dependence of the Electron Mean Free Path. *Surf. Interface Anal.,* **1980**, 2, 53-55

[48] NIST Standard Reference Database 20, Version 3.4

[49] Glatzel, P.; Bergmann, U.; High Resolution 1s Core Hole X-ray Spectroscopy in 3d Transition Metal Complexes Electronic and Structural Information. *Coord. Chem. Rev.* **2005**, 249, 65.

[50] Moretti Sala, M.; Martel, K.; Henriquet, C.; Al Zein, A.; Simonelli, L.; Sahle, C.; Gonzalez, H.; Lagier, M.-C.; Ponchut, C.; Huotari, S.; Verbeni, R.; Krisch, M.; Monaco, G.; A High-Energy-Resolution Resonant Inelastic X-ray Scattering Spectrometer at ID20 of the European Synchrotron Radiation Facility. *J. Synchrotron Rad.* **2018**,. 25, 580-591.

[51] Filipponi, A.; Di Cicco, A.; X-ray Absorption Spectroscopy and *n*-Body Distribution Functions in Condensed Matter. II. Data Analysis and Applications. *Phys. Rev. B* **1995**, 52, 15135.

[52] Borowski, M.; Size Determination of Small Cu-Clusters by EXAFS. *J. Phys. IV* **1997**, 7, C2–259.

[53] Calvin, S.; Luo, S. X.; Caragianis-Broadbridge, C.; McGuinness, J. K.; Anderson, E.; Morrison, S. A.; Kurihara, L. K.; Comparison of extended x-ray absorption fine structure and Scherrer analysis of x-ray diffraction as methods for determining mean sizes of polydisperse nanoparticles. *Appl. Phys. Lett.* **2005**, 87, 233102.

[54] Calvin, S.; Riedel, C. J.; Carpenter, E. E.; Morrison, S. A.; Stroud, R. M.; Harris, V. G.; Estimating Crystallite Size in Polydispersed Samples using EXAFS. *Phys. Scr.***2005**, 744.

[55] Joly, Y.; X-ray Absorption Near-Edge Structure Calculations Beyond the Muffin-Tin Approximation. *Phys. Rev. B* **2001**, 63, 125120.

[56] Guda, S. A.; Guda, A. A.; Soldatov, M. A.; Lomachenko, K. A.; Bugaev, A. L.; Lamberti, C.; Gawelda, W.; Bressler, C.; Smolentsev, G.; Soldatov, A. V.; Joly, Y.; Optimized Finite Difference Method for the Full-Potential XANES Simulations: Applicationto Molecular Adsorption Geometries in MOFs and Metal-Ligand Intersystem Crossing Transients. *J. Chem. Theory Comput.* **2015**, 11, 4512–4521.

[57] Balerna, A.; Bernieri, E.; Picozzi, P.; Reale, A.; Santucci, S.; Burattini, E.; Mobilio, S.; Extended X-ray-absorption Fine-Structure and Near-Edge-Structure Studies, on Evaporated Small Clusters of Au. *Phys. Rev. B*, **1985**, 31, 5058-5065.

[58] Balerna, A.; Mobilio, S.; Dynamic Properties and Debye Temperatures of Bulk Au and Au Vlusters Studied Using Extended X-ray-Absorption Fine-Structure Spectroscopy. *Phys. Rev. B* **1986**, 34, 4, 2293-2298.

[59] Zhang, P.; Sham, T. K.; X-Ray Studies of the Structure and Electronic Behavior of Alkanethiolate-Capped Gold Nanoparticles: The Interplay of Size and Surface Effects. *Phys. Rev. Lett.* **2003**, 90, 245502.

[60] Zhang, P.; Sham,T. K.; Tuning the Electronic Behavior of Au Nanoparticles with Capping Molecules. *Appl. Phys. Lett.* **2002**, 81, 736.

[61] Casaletto, M. P.; Longo, A.; Martorana, A.; Prestianni, A.; Venezia, A. M.; XPS Study of Supported Gold Catalysts: The Role of Au^0 and $Au^{+\delta}$ Species as Active Sites, *Surf. and Interface Anal*, **2006**, 38, 215,218.

[62] Schilling, C.; Hess, C.; Elucidating the Role of Support Oxygen in the Water−Gas Shift Reaction over Ceria-Supported Gold Catalysts Using Operando Spectroscopy *ACS Catal.* **2019**, 9, 1159−1171.

[63] Lohrenscheit, M.; Hess, C.; Direct Evidence for the Participation of Oxygen Vacancies in the Oxidation of Carbon Monoxide over Ceria-Supported Gold Catalysts by using Operando Raman Spectroscopy, *ChemCatChem* **2016**, 8, 523–526.

[64] Guzman, J.; Carrettin, S.; Fierro-Gonzalez, J. C.; Hao, Y.; Gates, B. C.;

Corma, A.; CO Oxidation Catalyzed by Supported Gold: Cooperation between Gold and Nanocrystalline Rare-Earth Supports Forms Reactive Surface Superoxide and Peroxide Species, *Angew. Chem. Int. Ed.* **2005**, 44, 4778–4781.

[65] Han, Z. K.; Wang, Y. G.; Gao, Y.; Catalytic Role of Vacancy Diffusion in Ceria Supported Atomic Gold Catalyst, *Chem. Commun.*, **2017**, 53, 9125.

[66] Joly, Y.; Electron Population Analysis by Full-Potential X-Ray Absorption Simulations. *Phys Rev Letter*, **1999**, 82, (11) 2398-2401.

[67] Merkulova, M.; Mathon, O.; Glatzel, P.; Rovezzi, M.; Batanova, V.;Marion, P.; Boiron, M.C.; Manceau, A.;*ACS Earth Space Chem.*, **2019**, 3 (9), pp.1905-1914.

[68] Chang, M. W.; Zhang, L.; Davids, M.; Filot, I. A. W.; Hensen, E. J. M.; Dynamics of Gold Clusters on Ceria During CO Oxidation. *J. Catal.* **2020**, 392, 39–47.

TOC

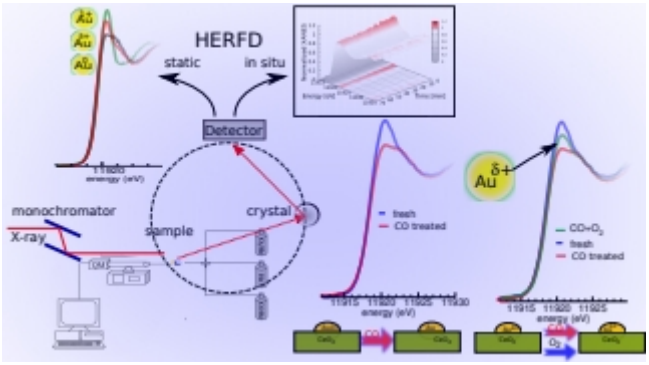

The Dynamic Role of Gold d-orbitals during CO oxidation under aerobic conditions.

Supporting information:

The Dynamic Role of Gold d-Orbitals During CO Oxidation Under Aerobic Conditions

Alessandro Longo[1,2*], Francesco Giannici[3], Maria Pia Casaletto[2*], Mauro Rovezzi[1,4], Christoph J. Sahle[1], Pieter Glatzel[1], Yves Joly[5], Antonino Martorana[3].

[1] ESRF - The European Synchrotron, CS 40220, 38043 Grenoble Cedex 9, (France).

[2] Istituto per lo Studio dei Materiali Nanostrutturati, Consiglio Nazionale delle Ricerche, Via Ugo La Malfa 153, 90146 Palermo, (Italy).

[3] Dipartimento di Fisica e Chimica, Università di Palermo, Viale delle Scienze, I - 90128 Palermo, (Italy).

[4] Universitè Grenoble Alpes, CNRS, IRD, Irstea, Météo France, OSUG, FAME, 71 Avenue des Martyrs, CS 40220, 38043, Grenoble (France).

[5] Universitè Grenoble Alpes Inst NEEL, 38042 Grenoble (France) and CNRS, Inst NEEL, 38042 Grenoble (France).

Corresponding Authors

** Alessandro Longo, alessandro.longo@esrf.fr*

** Maria Pia Casaletto, mariapia.casaletto@cnr.it*

SUPPLEMENTARY TEXT

Sample preparation

Au/CeO_2 powders, with Au loading of 1.0 and 3.0 % w/w determined by ICP-AES, were prepared by homogeneous deposition/precipitation method, using urea as precipitating agent. In a typical synthesis, 1 g of ceria (Aldrich, surface area = 79 m^2/g) was added to 100 mL of an aqueous solution containing $HAuCl_4$ (5×10^{-4} M) and urea in a urea/Au = 100 molar ratio. The suspension was kept at 353 K under stirring for 16 hrs, in order to favour urea decomposition with a gradual rise of pH until ~7. The solid was, then, filtered, washed with water until no chloride ions were detected by the $AgNO_3$ test, and dried in air at 393 K for 24 hrs.

X-ray Diffraction (XRD)

XRD measurements were carried out with a Bruker D5000 equipped with a Cu anode (Kα radiation λ=1.5418 Å) and a graphite monochromator. A proportional counter and a 0.05° step size in 2θ were used. The assignment of the crystalline phases was based on the JPDS database. As shown in the XRD patterns of the Au ceria supported catalysts in Figure S1, no evidences of metal particles were detected. They were only visible in the SAXS WAXS measurements collected using the synchrotron beam line DUBBLE at the ESRF facility, as shown in Figure S2.

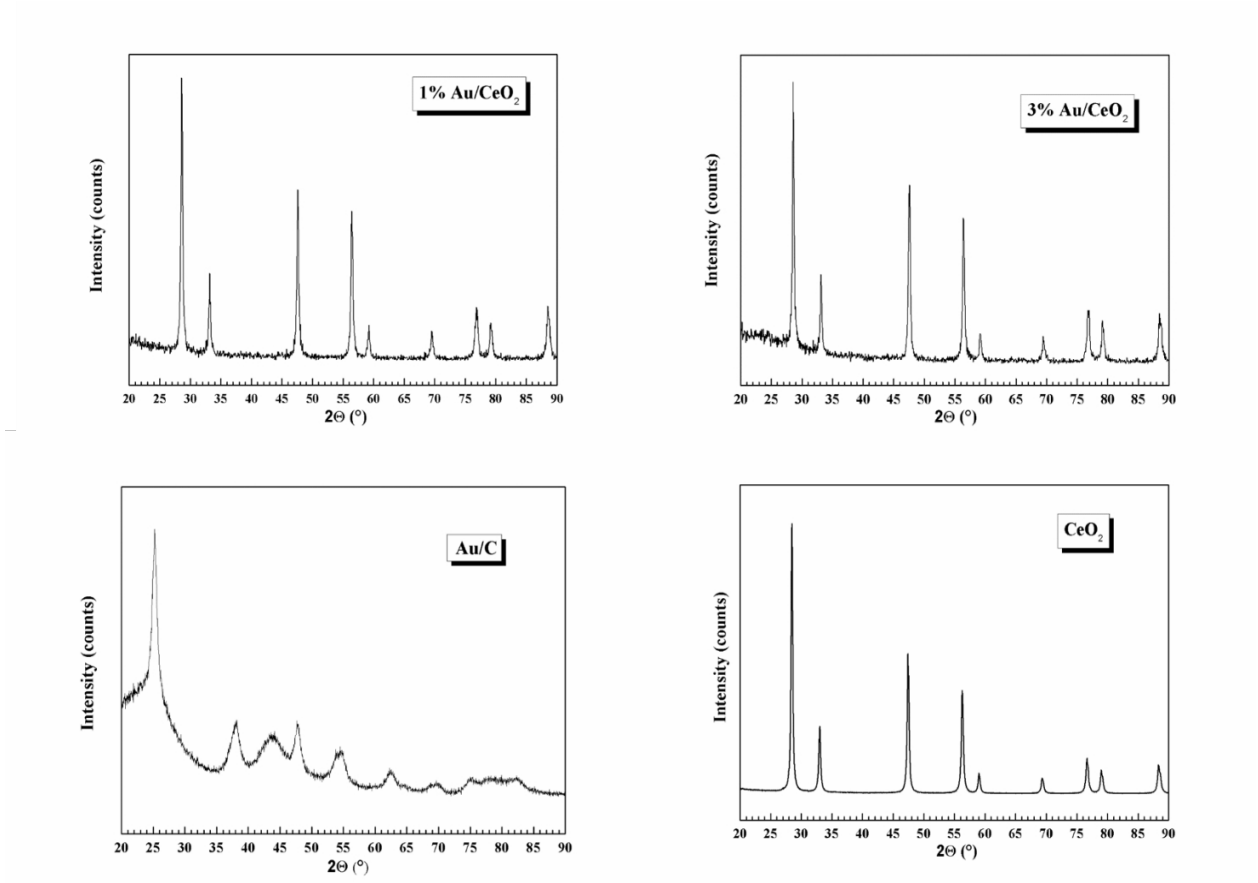

Figure S1. XRD patterns of 1% Au/CeO_2, 3% Au/CeO_2, Au/C catalysts and pure CeO_2 support, collected in laboratory.

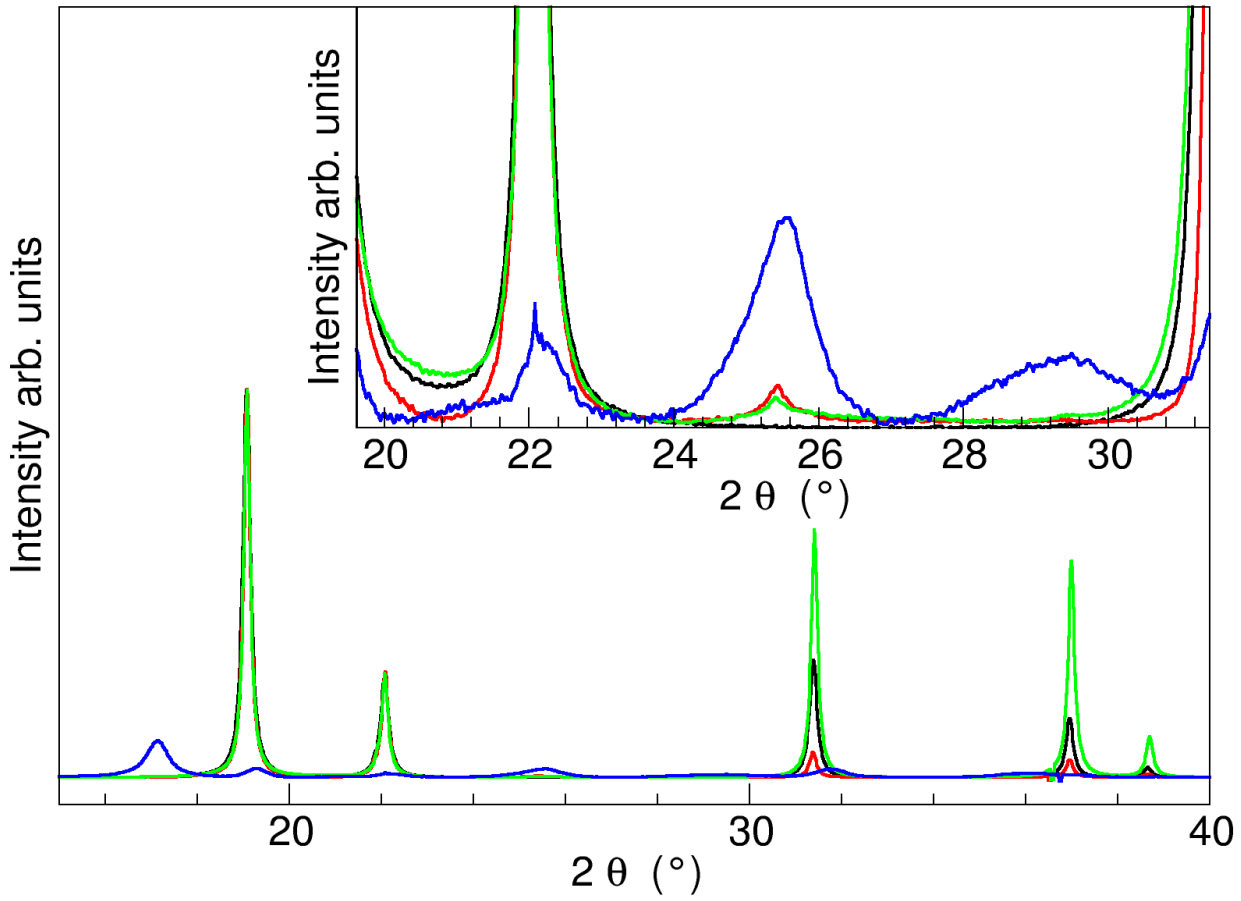

Figure S2. WAXS patterns of 1% Au/CeO_2, 3% Au/CeO_2, Au/C catalysts and pure CeO_2 support, collected at DUBBLE beamline at ESRF.

TABLE S1. Sherrer analysis of the XRD data collected at DUBBLE beamline at ESRF. Error is 0.3 nm for the size according to ref. [1].

SAMPLE	θ1 (◦)	θ2 (◦)	FWHM1 (◦)	D1 nm	FWHM2 (◦)	D2 nm	D1 Weight %	D2 Weight%
1% Au/C	25.25	-	0.6	8	-	-	-	-
1%Au/CeO_2	25.42	25.47	1.2	4.5	0.3	15	67	33
3%Au/CeO_2	25.75	25.51	1.4	4.2	0.2	20	73	27

SAXS modeling

Direct methods were used to get information on the size and arrangement of nanoscaled objects from SAXS data. Hence, a fitting of the purely mathematical Fourier transforms to the scattering intensities of non-interacting sphere system was performed. Accordingly, the intensity I(q) is

$I(q)=I_0V_0^2P(q)$ with q being the modulus of the scattering vector equal tp $4\pi\sin(\theta)/\lambda$; V_0 the volume of the particle; P(q) the form factor. I_0 contains experimental parameters, such as the scattering contrast, the beam intensity and additional variables due to the experimental setup. In the case of non-interacting system with some polydispersity, then the intensity can be written [2]:

$$I(q)=k\int_0^\infty D(r)\,j^2(qr)\,r^6\,dr+Background \qquad \text{eq. (1)}$$

where k is proportion factor; D(r) is the distribution function; j(qr) is the first order spherical Bessel function given by:

$$j_1(qr)=3\frac{\sin(qr)-qrcos(qr)}{qr^3} \qquad \text{eq. (2)}$$

D(r) in this case is the Weibull distribution function given by:

$$D(r)=\frac{b}{R}\left(\frac{r}{R}\right)^{(b-1)}\exp-\left(\frac{r}{R}\right)^b \qquad \text{eq. (3)}$$

where R is the scale parameter of the distribution function and b is the shape parameter. The background in this case is the SAXS pattern of the bare support, either ceria or carbon, whose weight is a free parameter in the fitting procedure.

The R mean of the Weibull distribution function is given by:

$$R_{mean}=R\Gamma\left(1+\frac{1}{b}\right) \qquad \text{eq. (4)}$$

The results of the fitting of the experimental data, performed by using a home-made minimization procedure involving MINUIT [3] package program, is reported in Table S2.

Table S2. Fitting parameters of SAXS analysis. The corresponding chi squared function χ^2 expressing the goodness of fit is also reported.

SAMPLE	R_{mean}(nm)	b	Background weight%	Reduced χ^2
1% Au/C	1.72±0.05	1.81±0.02	0.97±0.01	0.91
1% Au/CeO_2	1.41±0.05	1.9±0.05	0.98±0.02	0.96
3% Au/CeO_2	1.33±0.05	1.82±0.05	0.96±0.02	0.94

Atomic Force Microscopy (AFM)

1% Au/CeO_2 sample

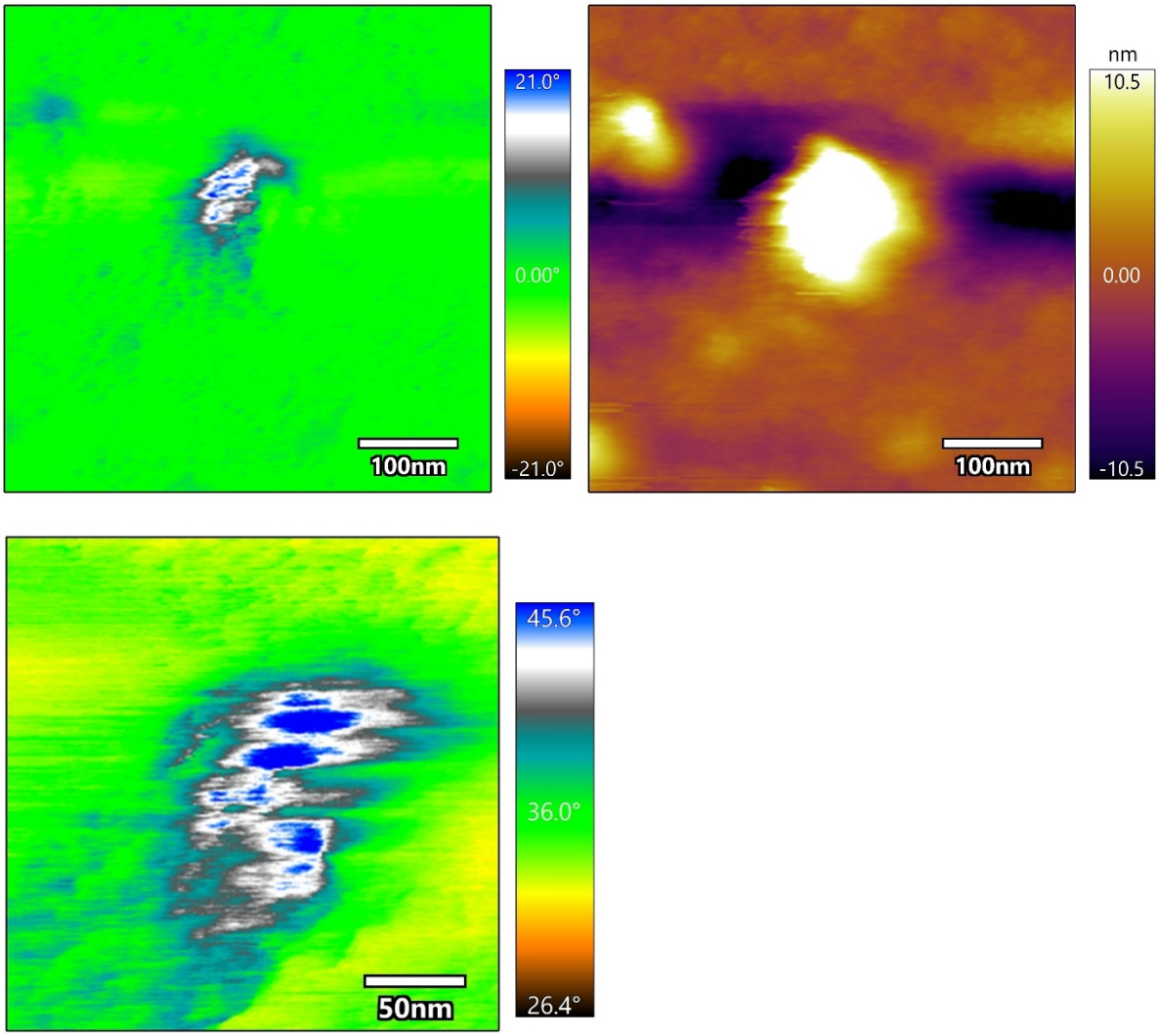

Figure S3. EFM pass phase signal on 1% Au/Ceria and topography of the same particle.

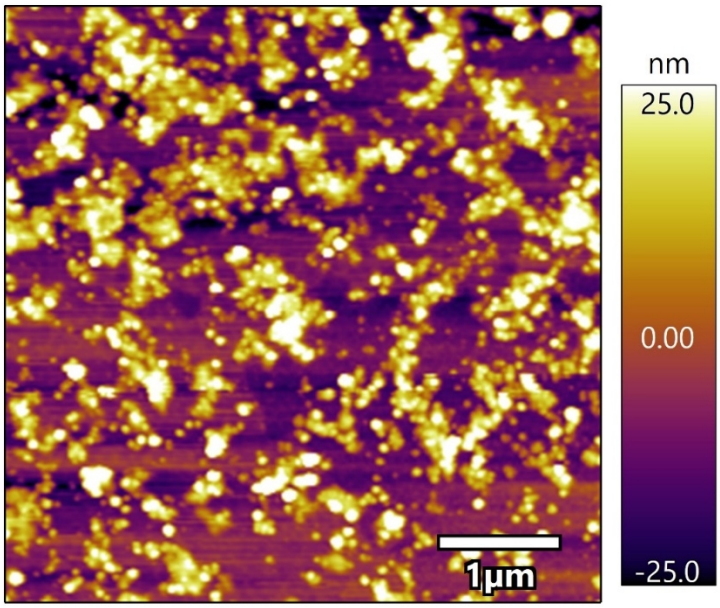

Figure S4. *Topography on the sample.*

3% Au/CeO_2 sample

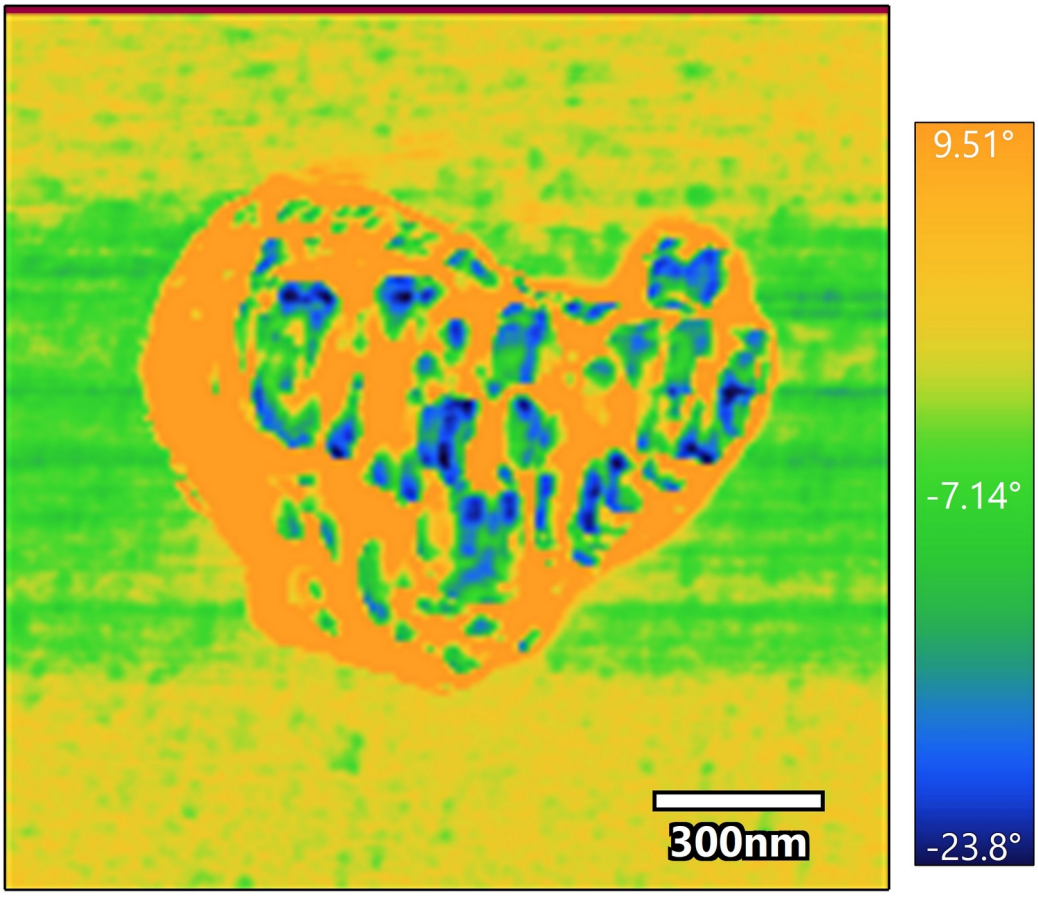

Figure S5. EFM pass phase signal on 3% Au/Ceria.

SEM and EDX

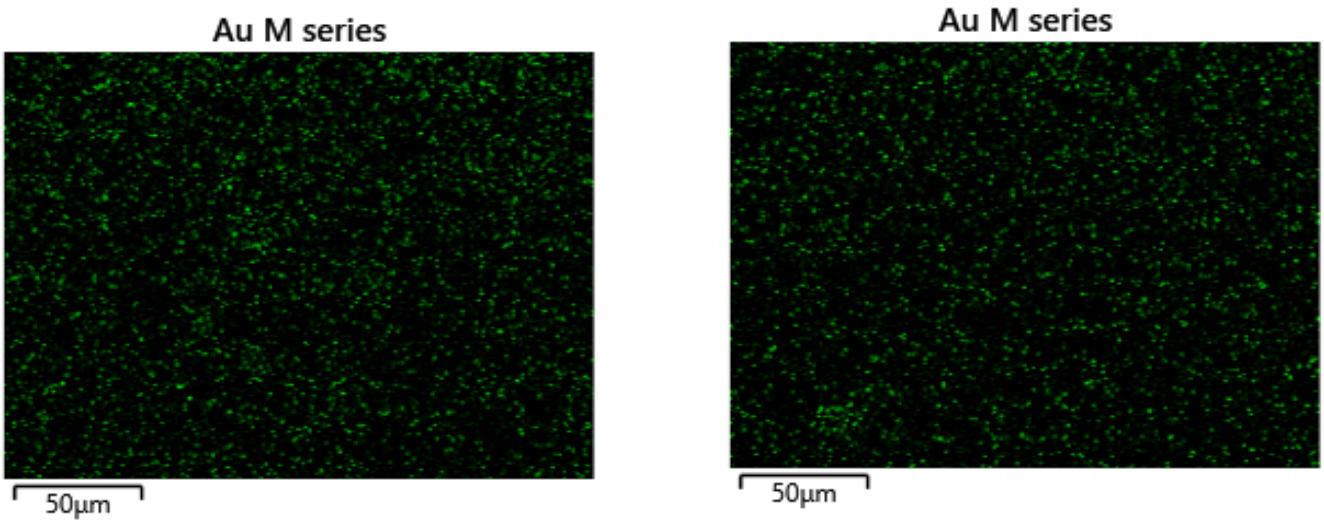

1% Au/CeO_2 **3%Au/CeO_2**

Figure S6. EDX of the 1% and 3% Au/CeO_2 catalysts.

X-ray photoelectron spectroscopy (XPS) and XPS data analysis

XPS analysis were performed by a VG Microtech ESCA 3000 Multilab spectrometer equipped with a dual Mg/Al anode. Spectra were acquired by using a non-monochromatized Al K_α source (hv= 1486.6 eV), a five-channeltrons detection system and an electron hemispherical analyzer operating in constant analyzer energy (CAE) mode atpass energy of 20 eV. Sample powders were pelletized and then mounted on a graphite adhesive tape. The pressure in the analysis chamber was in the range of 10^{-8} Torr during data collection. The binding energy scale (BE) was charge compensated by using C 1s peak (BE = 285.1 eV) from adventitious carbon. The accuracy of energy measure is ± 0.1 eV. In order to rule out a partial reduction of gold species while recording XPS data, Au spectra were acquired at the beginning and at the end of the analyses and the invariance of the peak shapes and widths ascertained the absence of differential surface charging. The analysis of XPS spectra was performed by a nonlinear least

square curve-fitting procedure allowing to separate elemental species in different oxidation states. A properly weighted sum of Lorentzian and Gaussian component for the shape of Voigt curves was used, after Shirley background subtraction according to Sherwood.

Results of XPS analysis (see Figure S7) evidenced that the curve-fitting of the Au 4f signal in the 3%Au/CeO_2 sample consisted of a single Au $4f_{7/2}$ component located at a binding energy BE = 84.5 eV, typically assigned to Au^0 metallic gold species [see ref. 37, 39, 59 in the main text]. The corresponding Au $4f_{5/2}$ component was found at BE = 88.1 eV. No evidence of oxidized gold species was detected by XPS on the surface of the 3%Au/CeO_2 sample. The curve-fitting of the Au 4f signal in the 1%Au/CeO_2 sample consisted of a predominant Au $4f_{7/2}$ component located at a binding energy BE = 84.4 eV, typically assigned to Au^0 metallic gold species. The other small component located at BE = 85.5 eV is attributed to the presence of surface Au^{+1} species [see refs. 37, 39, 59 in the main text], corresponding to about 25% of gold total peak area (see Table S3). The relative surface chemical composition of the investigated samples determined by XPS is reported in Table S3 and expressed as atomic percentage (atom. %).

Table S3. XPS surface chemical composition of the investigated samples (atom. %)

SAMPLE	Au 4f	Ce 3d	O 1s	C 1s
1% Au/CeO_2	0.2	18.1	35.1	46.6
3% Au/CeO_2	0.9	20.6	34.2	44.3

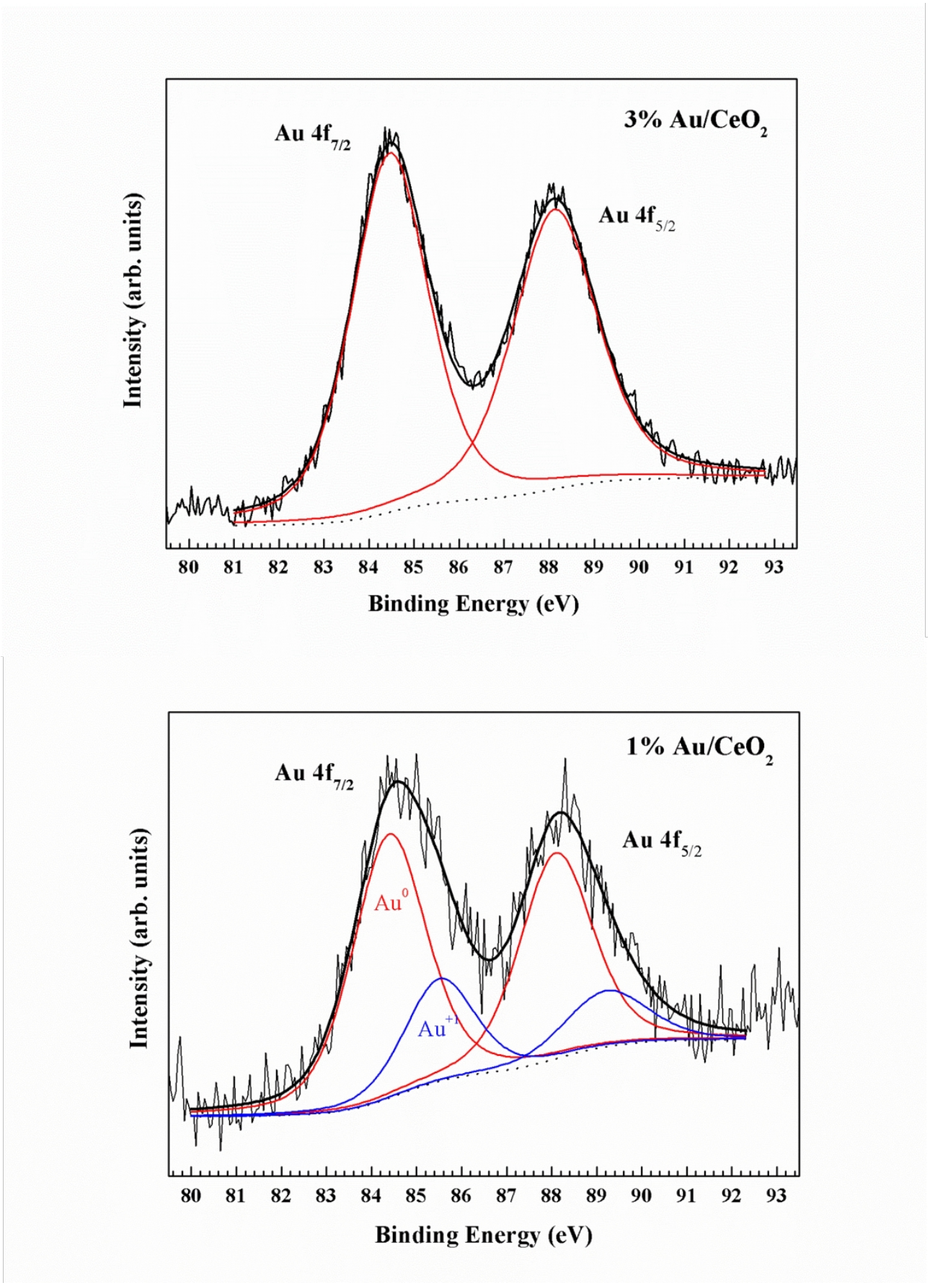

Figure S7. XPS curve-fitting of Au 4f spectra in the investigated samples.

In situ HERFD-XAFS

X-ray absorption spectroscopy measurements were carried out at the high-brilliance XAFS-XES beamline ID26 and at the inelastic scattering beamline ID20 of the European Synchrotron Radiation Facility (ESRF) in Grenoble, France [4]. *In situ* and *ex situ* HERFD-XAFS measurements were performed at room temperature using the “microtomo reactor”. The measurements were performed using the third harmonic of two u35 undulators. The monochromator was equipped with a pair of Si(220) single crystals. Higher harmonics were suppressed by two Cr-coated mirrors operating at 3 mrad relative to the incident beam. The energy was calibrated using an Au foil. The high-energy-resolution fluorescence detection was performed using a horizontal-plane Rowland circle spectrometer and several photodiodes (APD, Perkin-Elmer) as detectors. The spectrometer was tuned to the Au La1 (9713 eV) fluorescence line by using the (660) Bragg reflection of one spherically bent Ge wafer with R=1 m and a diameter of 89 mm. The energy resolution of the spectrometer was 0.3 eV. A Canberra Si photo-diode was mounted to measure the total fluorescence yield simultaneously. During HERFD-XANES scans, the undulators were kept at a fixed gap and only the monochromator angle was changed. The beam-size was 0.5hx0.1v mm square. Some samples were also remeasured at Id20 in the RIXS branch [5]. The incident radiation was monochromatized by a high heatload double crystal Si(111) monochromator and a postmonochromator for further bandwidth reduction. In the high energy-resolution mode, a Si(311) back-scattering channel-cut reduced the incident photon bandwidth. The scattered X-rays were energy-analyzed by a Rowland-type spectrometer, equipped with the Si(951) as crystals analyzers.

During the *in situ* measurements, evolution of CO_2 was monitored by a mass quadrupole connected to the outlet of the cell. Figure S8 show the typical

behaviour of the gas concentration during the experiments described in the main manuscript. Notably, the monitoring of the CO_2 is mandatory to link the d band evolution with the CO oxidation. However, the set-up of the cell, that was fully optimized for the HERFD-XANES, was not ideal to interpret the kinetic study as reported elsewhere. [refs 16, 26 in the main text]. So, the mass quadrupole information merely indicates the occurrence of CO oxidation.

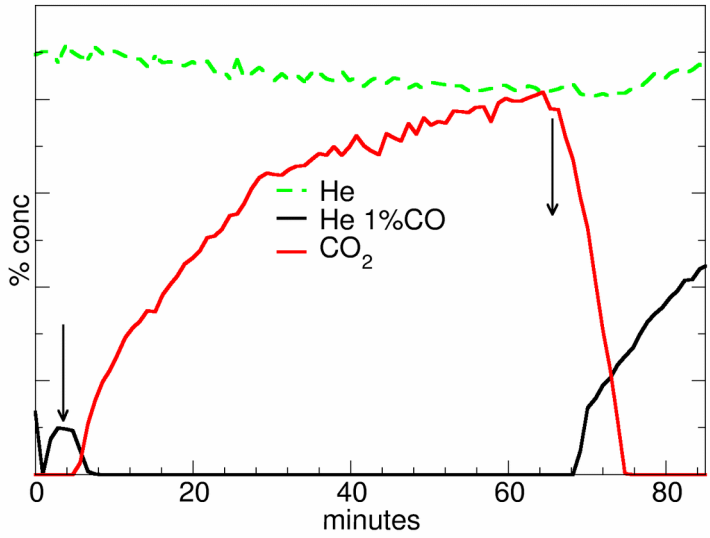

Figure S8. Gas concentration during CO oxidation on 3% Au/CeO_2 catalyst at RT registered by a mass quadrupole. The arrows indicate the time when the He 1%CO gas mixture started flowing in the cell (left) and when it was switched off (right).

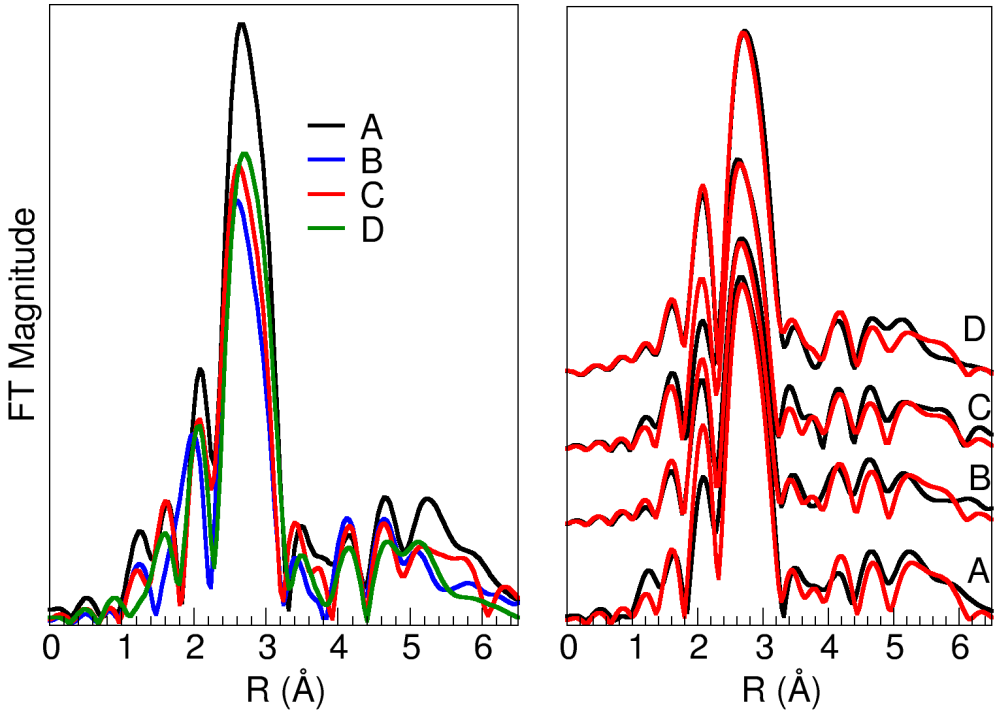

Figure S9. Fourier transform of the EXAFS signals of: gold foil (A), 1% Au/CeO_2 fresh catalyst (B), 1% Au/CeO_2 CO treated catalyst (C) and 1% Au/C catalyst (D) reported for comparison.

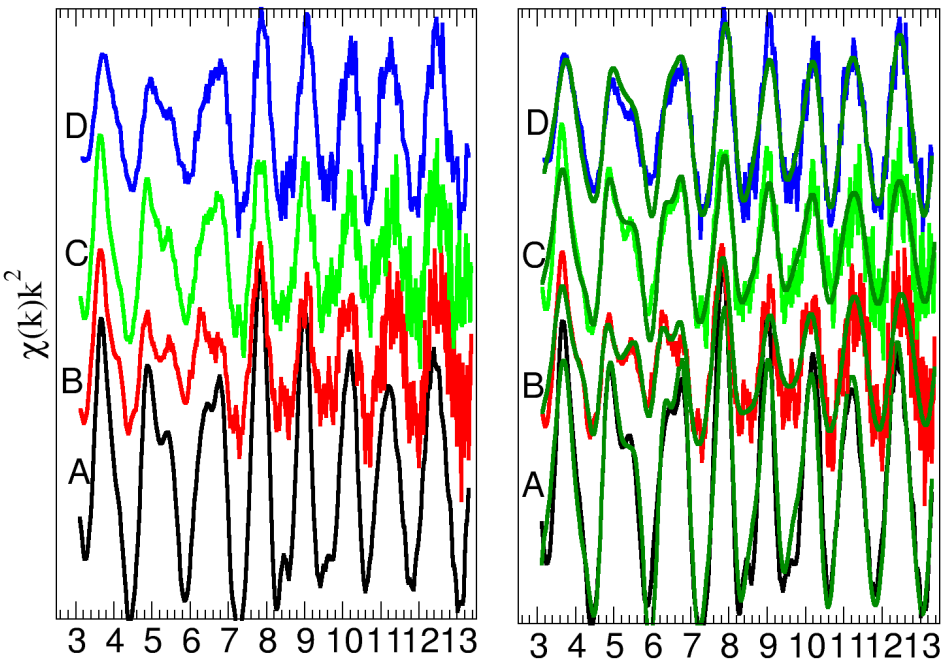

Figure S10. EXAFS signals for: gold foil (A), 1% Au/CeO_2 fresh catalyst (B), 1% Au/CeO_2 CO treated catalyst (C) and 1% Au/C catalyst (D).

Table S4. The fitting parameters used in the minimization procedure are reported in bold case, whereas the calculated structural parameters in italic. All distances are in Å and all Debye−Waller factors in $Å^2$. Angles are in degree. The errors of the fitting parameters are reported in parentheses. G is the agreement factor of the fitting as defined in ref. [6].

	Au foil	**1% Au/C**	**1% Au/CeO_2**	**3% Au/CeO_2 CO**
E0	11919.0 (0.5)	11918.8(0.5)	11918.7(0.5)	11910.1(0.5)
N1	12	10.3(0.8)	10.6(0.8)	9.5(0.8)
R1	2.877 (0.01)	2.85 (0.01)	2.86 (0.01)	2.86 (0.01)
σ1	0.0052(0.0005)	0.0069 (0.0005)	0.0095 (0.0005)	0.0091 (0.0005)
N2	6	4.0	4.0	4.1
R2	4.07 (0.02)	4.03 (0.02)	4.05 (0.02)	4.05 (0.02)
σ2	0.0077 (0.0005)	0.0075 (0.0005)	0.012(0.001)	0.013 (0.001)
θ1	120	120	120	120
R3	4.95	4.93	4.95	4.96
N3	24	14	15	15
θ2	180 (1)	179 (1)	181 (4)	180 (5)
R4	5.75	5.72	5.73	5.75
N4	12	6.3	6.5	6.7
D clusters (nm)	-	2.7 (0.7)	2.4(0.8)	2.2 (0.8)
G	**0.25E-05**	**0.31E-05**	**0.59-05**	**0.32E-05**
G expected	**0.11E-06**	**0.80E-05**	**0.30E-05**	**0.12E-05**

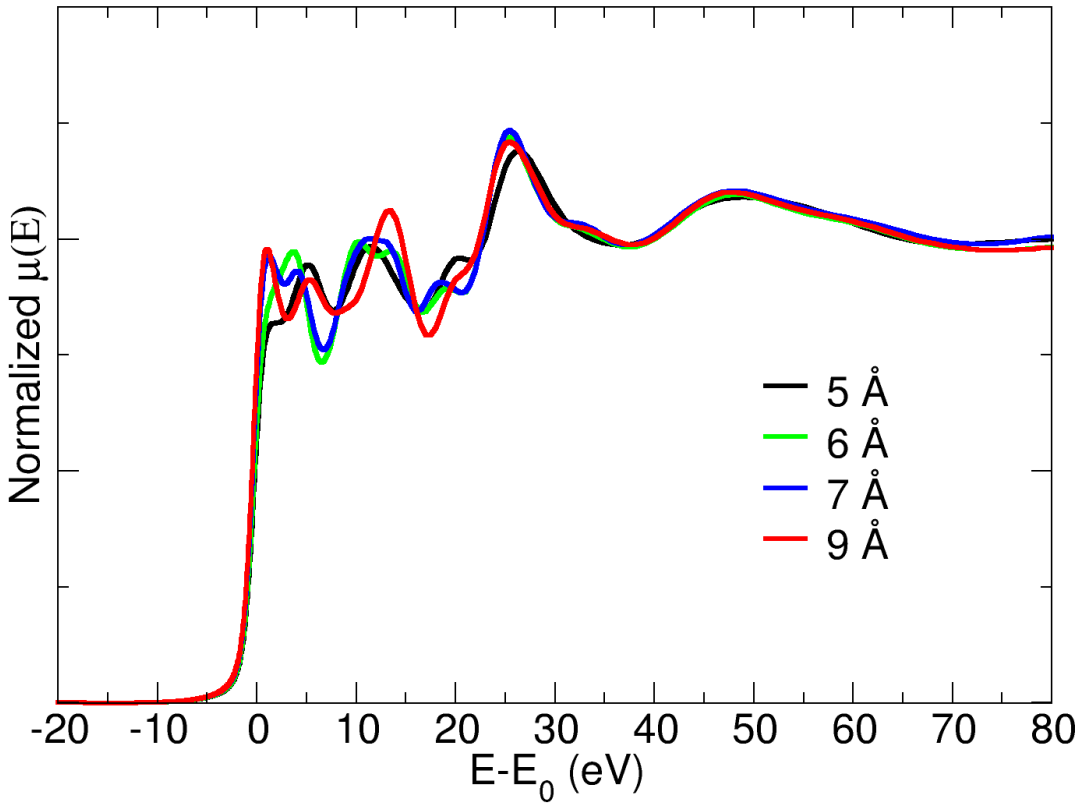

Figure S11. XANES calculations repeated for different clusters radii from 5 to 9 Å.

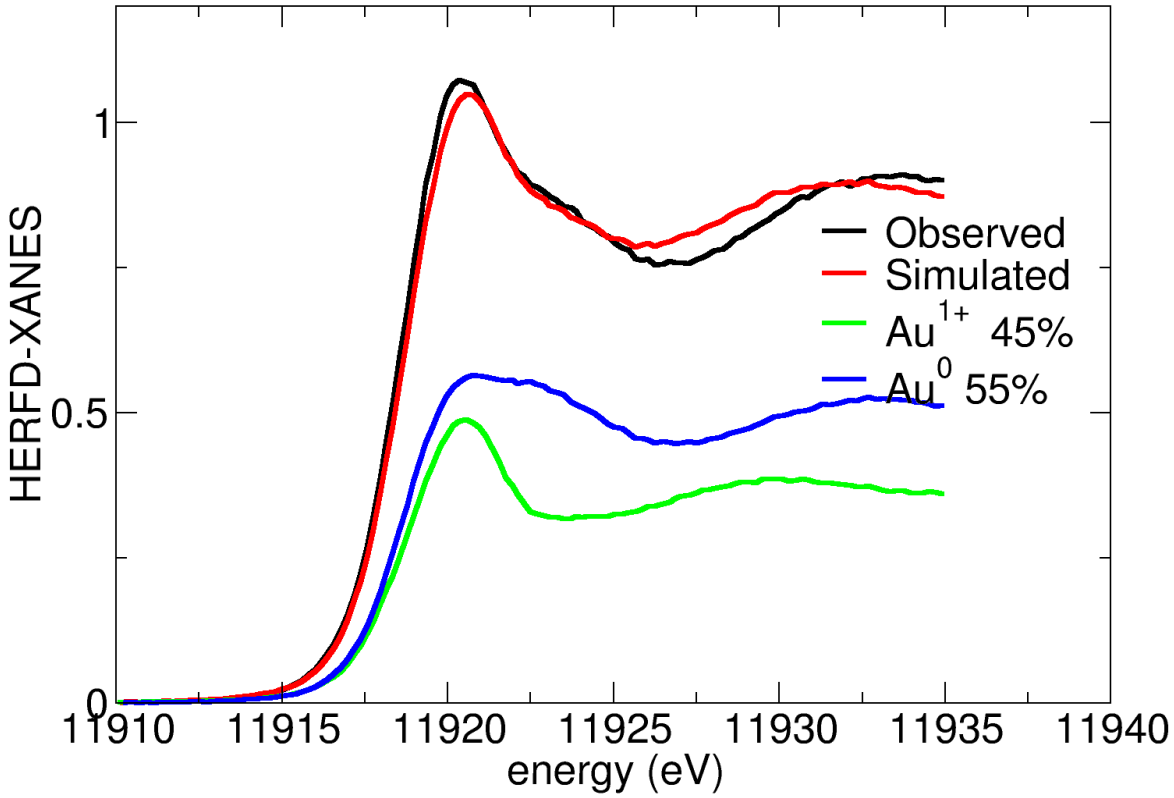

Figure S12. Simulation of the HERFD-XANES spectrum of 3% Au/CeO_2 catalyst by using AuL, $(C_2H_5)_3PAuCl$ as reference spectrum to simulate the Au^{1+} component (green line) and Au deposited on C as reference for the Au^0 metallic component.

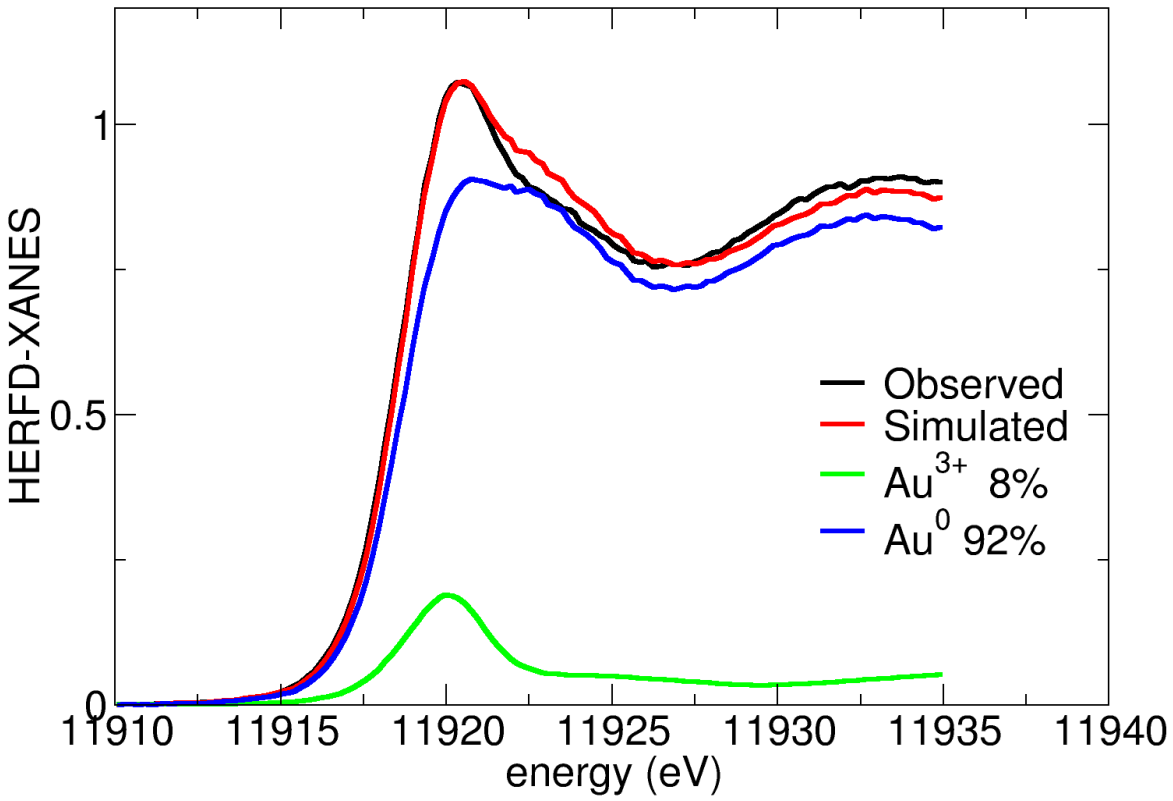

Figure S13. Simulation of the HERFD-XANES spectrum of 3% Au/CeO_2 catalyst by using $AuCl_3$ spectrum as a reference to simulate the Au^{3+} component (green line) and Au deposited on C as reference for the Au^0 metallic component.

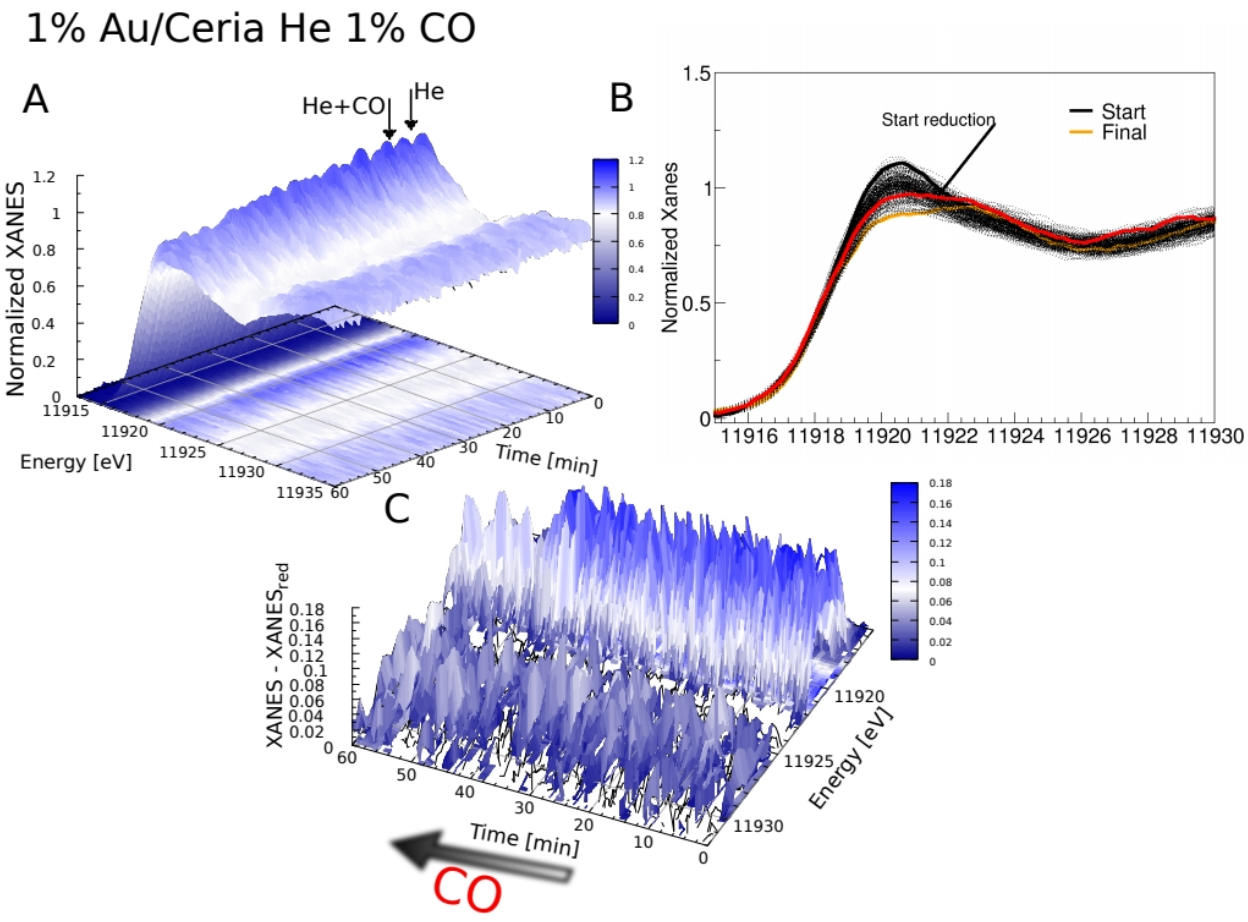

Figure S14. Panel A: Evolution of HERFD-XANES spectra of 1% Au/CeO_2 catalyst during the CO treatment. Panel B:-Superimposed XANES spectra, of 1%Au/CeO_2 and 1%Au/C during the CO reduction. Panel C: Relative intensity of the peak maximum minus the averaged reduced spectrum.

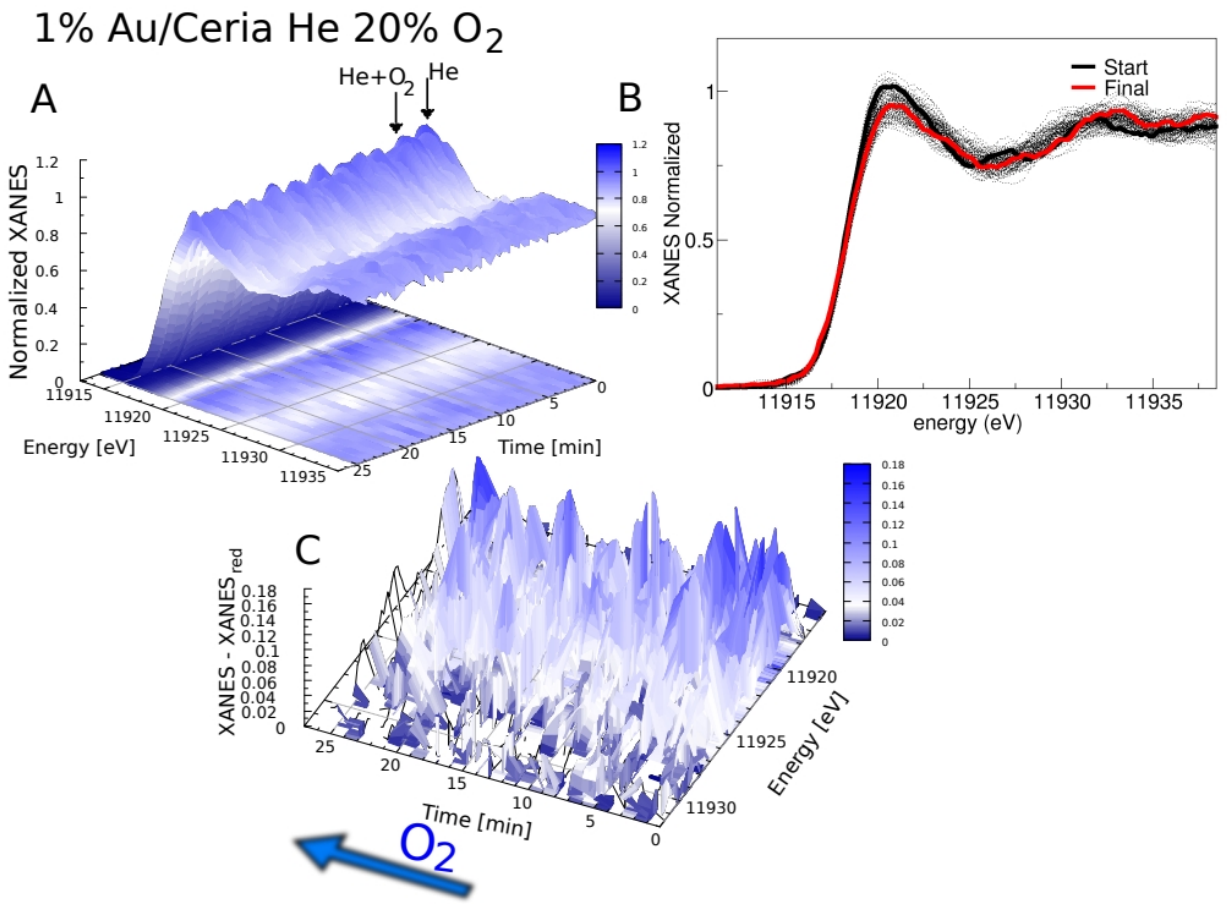

Figure S15. Panel A: Evolution of HERFD-XANES spectra of 1% Au/CeO_2 catalyst during the O_2 treatment. Panel B: Superimposed XANES spectra. Panel C: Relative intensity of the peak maximum minus the averaged reduced spectrum.

REFERENCES

[1] Vorokh, A. S.; Scherrer formula: estimation of error in determining small nanoparticle size. *Nanosystems: Phys. Chem. Math.* **2018,** 9(3), 364. DOI: https://doi.org/10.17586/2220-8054-2018-9-3-364-369.

[2] Longo, A.; Portale, G.; Small-Angle X-Ray Scattering for the Study of Nanostructures and Nanostructured Materials, 175-228, in "Characterization of Semiconductor Heterostructures and Nanostructures" , 2014, Elsevier Amsterdam.

[3] MINUIT is a Python interface to the MINUIT2 C++ package (standard tool at CERN): https://indico.cern.ch/event/833895/contributions/3577808/attachments/1927550/3191336/iminuit_intro.html

[4] Glatzel, P.; Bergmann, U.; High resolution 1s core hole X-ray spectroscopy in 3d transition metal complexes-electronic and structural information. *Coord. Chem. Rev.* **2005**, 249, 65.

[5] Moretti Sala, M.; Martel, K.; Henriquet, C.; Al Zein, A.; Simonelli, L.; Sahle, C.; Gonzalez, H.; Lagier, M.-C.; Ponchut, C.; Huotari, S.; Verbeni, R.; Krisch, M.; and Monaco, G. ; *J. Synchrotron Rad*. **2018**, 25, 580.

[6] Filipponi, A.; Di Cicco, A.; *X-ray-absorption spectroscopy and n-body distribution functions in condensed matter. II. Data analysis and applications Phys. Rev.* B **1995**, 52, 15135.